Title:

Tau interactions with inner nuclear envelope proteins modulates chromatin

Authors:

Lisa Diez[1]*, Renata Ponce-Lina[1]*, Rithika Sankar[1], Cagla Kilic[1,3], Cong Wang[4], Pia Grundschoettel[5,6], Koki Sakurai[7,8], Frieda Balduin[1], Bilge Askin[1,2,3], Chiara Bordier[1], Tejaswini Karra[1], Katharina Tipp[1], Leandre Ravatt[1,2,3], Boglarka Krisztina Nagy-Herczeg[1], Alvaro Dominguez-Baquero[1,3], Ramesh Adakkattil[9] , Sabrina Hübschmann[1], Satabdee Mohapatra[1,3], Elena De Domenico[10], Marc Beyer[10], Tomohisa Toda[7,8,11], Helena Radbruch[12], Tara L. Spires-Jones[13,14], Alexander von Appen[9], Thomas Ulas[5,6], Andrew Newman[15], Fan Liu[4], Susanne Wegmann[1,2,3,#]

[1] German Center for Neurodegenerative Diseases (DZNE), Berlin, Germany
[2] Einstein Center for Neuroscience (ECN), 10117 Berlin, Germany
[3] Charité University Medicine, 10117 Berlin, Germany
[4] Department of Structural Biology, Leibniz-Forschungsinstitut für Molekulare Pharmakologie (FMP), 13125 Berlin, Germany
[5] Genomics and Immunoregulation, Life & Medical Sciences (LIMES) Institute, University of Bonn, Bonn, Germany
[6] Systems Medicine, German Center for Neurodegenerative Diseases (DZNE), Bonn, Germany
[7] Laboratory of Neural Epigenomics, Institute of Medical Physics and Micro-tissue Engineering, Friedrich-Alexander-Universität Erlangen-Nürnberg, 91054 Erlangen, Germany
[8] Max-Planck-Zentrum für Physik und Medizin, 91054 Erlangen, Germany
[9] Max Planck Institute of Molecular Cell Biology and Genetics, 01307 Dresden, Germany
[10] Platform for Single Cell Genomics and Epigenomics (PRECISE), DZNE Bonn, 53127 Bonn, Germany
[11] German Center for Neurodegenerative Diseases (DZNE), 01307 Dresden, Germany
[12] Department of Neuropathology, Charité Universitätsmedizin Berlin, 10117 Berlin, Germany
[13] UK Dementia Research Institute, the University of Edinburgh, Edinburgh EH8 9JZ, UK
[14] Centre for Discovery Brain Sciences, the University of Edinburgh, Edinburgh EH8 9JZ, UK
[15] Institute of Cell and Neurobiology, Charité Universitätsmedizin Berlin, 10117 Berlin, Germany

corresponding author: susanne.wegmann@dzne.de
* contributed equally

Keywords:

nucleus, nuclear envelope, interactome, proximity biotinylation, Lamin B receptor, DNA, heterochromatin, gene expression, phase separation, Alzheimer's disease, tauopathies

Abstract/Summary

Intracellular re-distribution of the neuronal microtubule associated protein Tau, from the axon into the somatodendritic compartment, is a physiological stress-related event that increases Tau in the soma and enables Tau interactions with the nucleus. Cellular functions of stress-induced Tau-Nucleus interactions are unknown. Combining proximity biotinylation interactomics with chromatin imaging and molecular reconstitution assays, we uncover that physiological Tau interacts with proteins coordinating chromatin at the nuclear membrane, including lamin B receptor, thereby changing their DNA interactions. Accordingly, we find that increasing somatodendritic Tau is sufficient to dysregulate expression of genes in lamin associated domains and transcription factors, collectively leading to an upregulation of stress response pathways and downregulation of cholesterol metabolic genes. These nuclear envelope-related mechanisms suggest that neuronal stress-related somatodendritic Tau missorting can initiate chromatin-related cascades important for early changes in AD and tauopathies.

Introduction

Tau, encoded by the *MAPT* gene, is an intrinsically disordered protein that has a high affinity to microtubules (MTs)[1,2]. The majority of Tau is expressed in neurons of the central nervous system. In mature neurons, Tau is enriched in the axon where its microtubule association is regulated by phosphorylation and other post-translational modifications (PTMs)[1]. In conditions where Tau gets "activated", the subcellular distribution of phosphorylated Tau – detached from MTs – changes, and similar levels of soluble cytosolic Tau can be found throughout axon, soma, and dendrites. This subcellular Tau redistribution can be triggered by various physiological neuronal stress conditions, including temperature changes, mechanical stimulation, and neuronal hyperactivity[2–4].

In the brain, pathological accumulation of phosphorylated Tau in neuronal cell bodies can be observed in a number of (>20) neurological conditions, e.g., in traumatic brain injury, epilepsy, autoimmune brain diseases, and – most prominently – in Alzheimer's disease (AD) and tauopathies[5,6]. It is widely believed that accumulation of soluble phospho-Tau precedes Tau aggregation in neuronal cell bodies, which is a pathological hallmark and correlate of neuronal loss in these diseases. The actual, neurophysiological reason and consequence for the initial somatodendritic Tau "resorting" in neuronal stress situations remains unclear.

Soluble Tau seems to be involved in many "alternative" functions[7,8]. It is likely that the interaction of Tau with molecules and organelles in the somatodendritic compartment builds the foundation for stress-related Tau functions. For example, interactions of Tau with the neuronal nucleus are enabled by its redistribution into the soma, both in physiological stress and in disease conditions.

In AD and FTD, Tau misfolding and aggregation correlate with changes in chromatin and gene expression in human AD and tauopathy brains, as well as in tauopathy animal models[9–11]. Global chromatin relaxation[10], neurotoxic re-activation of retroviral transposable elements[12,13], and activation of senescence-like expression profiles[14] have been reported as consequences of Tau aggregation in the brain. In addition, Tau clusters at the outer nuclear envelope (NE) were suggested to impair nuclear transport through nuclear pores in AD brains[15–19] and thereby could indirectly affect chromatin and gene expression. In the physiological context, Tau inside the nucleus was shown to interact with DNA, histone proteins, and the nucleolus[2,20–25] with suggested functions in gene expression, DNA protection and compaction, and nucleolar stress response. However, there is currently no consensus about the impact of Tau on chromatin; reported effects range all the way from Tau-induced global chromatin relaxation and transcriptional activation[10,26,27] to stabilization of chromatin compaction and transcriptional deactivation[9,22]. We propose that these inconclusive results – at least in part – result from difficulties to distinguish between physiological nuclear actions of soluble somatodendritic Tau *versus* pathological actions or loss of nuclear functions of oligomeric and aggregated Tau.

In this study, we set out to unravel the interactions of Tau with the nucleus and whether neuronal chromatin alterations are connected to Tau's re-distribution, i.e., its abundance in the somatodendritic compartment. The herein newly identified interactions of Tau with nuclear envelope proteins, like the lamin B receptor (LBR), provide a molecular mechanism for neuronal chromatin and gene expression alterations in response to physiological, stress-induced soluble Tau resorting. These findings provide an important missing link for understanding the transition from physiological function to pathological (mis)function of Tau in the brain.

Results

Pathological Tau distorts the nuclear envelope in the brain

In human Alzheimer's disease (AD) brains, immunolabeling showed the accumulation of misfolded (Alz50+) and aggregated Tau in the soma of neurons (Figure 1A,B). In neurons having soluble phospohrylated Tau (pS202/pS205/pT231), presumably prior to developing Tau aggregation pathogy, we could observe p-Tau at the nuclear enveleope (NE; labeled with anti-SUN1 antibody; Figure 1B). Neurons with cytosolic p-Tau aggregates (NFTs) did not show this

114 Tau pattern, indicating that cytosolic oligomeric Tau may have a special affinity to the NE. This
115 is line with previous observations of our own and others [17,18,38].
116 In addition, we observed an increased number of neuronal nuclei having NE deformations –
117 folds and invaginations – in AD (Braak 5/6) compared to control (Braak 0/1) brains, whereby
118 the occurrence of invagination was higher in neuorns with misfolded Tau in the soma (Figure
119 1C,D; Supplemental Video V1-4). In both AD and control brains, the number of nuclei
120 surrounded by aggregated Tau correlated with the number of neuronal nuclei with
121 invaginations (Figure 1E). Tau-induced nuclear envelope deformations could, for example, be
122 due to MT polymerizing aberrantly through the NE in tauopathies[39], or due to impaired
123 cytoskeletal force transduction caused by deficits in LINC complex components[27]. The details
124 of Tau interactions with the NE, and their consequences, remain unclear though.
125
126 ***Nuclear Tau interactomics identifies nuclear envelope proteins***
127 To understand the interactions of somatodendritic Tau with the nuclear envelope, we
128 systematically identify nuclear interaction partners of Tau that could be involved in chromatin
129 regulation, we performed proximity biotinylation Tau interactomics. We fused full-length human
130 wildtype (TurboID-Tau) or mutant Tau^{P301L} (TurboID-Tau^{P301L}; Figure 2A,B) to the biotin ligase
131 TurboID[44], which facilitated the rapid (within minutes upon addition of excess biotin into the
132 culture medium) biotinylation of proteins in proximity (~35 nm distance) to Tau or Tau^{P301L} in
133 their native cellular environment. To enrich for potential nuclear interaction partners, we
134 transiently expressed TurboID-Tau and TurboID-Tau^{P301L} in human neuroblastoma cells (SH-
135 SY5Y line), lysed the cells in hypotonic buffer, and enriched the nuclei by centrifugation.
136 Biotinylated proteins were pulled down from the nuclear pellet using magnetic streptavidin-
137 coated beads and analyzed by mass spectrometry (Figure 2B,C,D; Supplemental Figure S1).
138 Expression of TurboID alone was utilized to obtain a control interactome for unspecific TurboID
139 activity. Notably, while the TurboID-Tau fusion constructs (MW ~85 kDa) mostly located to the
140 cytoplasm, the TurboID only control (MW ~39 kDa) was abundant in the nucleus due to its
141 smaller size (Figure 2C), rendering it a stringent control for identified nuclear Tau interactors.
142 As positive control and reference interactome for protein-specific nuclear interactions, we also
143 determined the interactome of TurboID fused to the C-terminal fragment of TDP-43 (TurboID-
144 TDP-43ctf; Figure 2A-D), a component of insoluble cytoplasmic TDP-43 aggregates in
145 ALS/FTD brains[45]. A proximity biotinylation interactome of TDP-43ctf has previously been
146 determined in mouse neuroblastoma cells[46], and we used these data here to verify the success
147 and specificity of our proximity biotinylation approach.
148 Proteomic analysis of biotinylated proteins from five independent biological replicates revealed
149 multiple significantly enriched proteins in the TurboID-Tau (87 proteins) and TurboID-Tau^{P301L}
150 (44 proteins) proximity proteome compared to TurboID alone (log2[fold change target/Ctrl]
151 >1.5, p-value <10^{-1}) (Figure 2E; Supplemental Tables T1, T2). As expected, Tau itself (MAPT)
152 was maximally enriched in Tau and Tau^{P301L} interactomes. Among the significantly enriched
153 proteins, we found 17 genes interacting with both Tau variants and TDP-43ctf (Figure 2F).
154 About ~30% of Tau interactors (27/87) and ~60% of Tau^{P301L} interactors (27/44) were shared
155 between the two Tau variants, whereas Tau had only 43% interactors in common with TDP-
156 43ctf (37/87) (Supplemental Table T3).
157 Pathway enrichment analysis (over-representation analysis (ORA) with gene ontology (GO)
158 categories *Cellular Components* for TurboID-Tau and TurboID-Tau^{P301L} over TurboID control;
159 Figure 2G) clustered the identified potential Tau interactors into the cellular compartments
160 "nuclear inner membrane" and "nuclear outer membrane". Tau^{P301L} had overall fewer
161 interactors that clustered in the categories "nuclear outer membrane" and "organelle
162 envelope". This suggested that the nuclear envelope (NE) plays an important role for nuclear
163 Tau interactions. Indeed, previous data indicated that Tau interactions with nuclear pore
164 proteins affect the neuronal nuclear transport in AD[38]. Here we find that Tau may interact not
165 only with several proteins involved in nuclear transport (nuclear pore proteins, Nups, and
166 nuclear transport receptors, NTRs), but also with NE proteins involved in chromatin
167 organization at the inner nuclear lamina (Figure 2H). Notably, since the NE is an extension of
168 the endoplasmic reticulum (ER), GO analysis for *Biological Processes* showed an enrichment

169 of endoplasmic reticulum (ER) proteins in the Tau, Tau^{P301L} and TDP-43ctf biotinylation
170 proteomes (Figure 2G; Supplemental Figure S1C; Supplemental Table T4). Identified NE-
171 specific proteins could be grouped into four protein categories (Figure 2I): (i) INM embedded
172 proteins (LBR (=lamin B receptor) and LEM-domain proteins, LEM2 and EMD (=Emerin)) that
173 coordinate chromatin association and repression at the inner leaflet of the NE[48], as well as
174 lamin associated inner nuclear membrane protein TMEM43 (LUMA), important for NE structure
175 and anchoring Emerin in the envelope[49]. (ii) Structural nuclear pore complex (NPC) proteins
176 (Nup210, NDC1) in the nuclear envelope-embedded ring of the NPC[50]. (iii) Components of the
177 LINC (linker of nucleoskeleton and cytoskeleton) complex (SYNE2 (=Nesprin-2), SUN1)
178 required to translate cytoskeletal mechanical forces into changes in chromatin structure and
179 gene expression [51,52]; (iv) Nuclear transport receptors (e.g., TNPO2 and XPO6) that regulate
180 the nuclear import and export, respectively, of biomolecular cargo through NPCs[53]. Notably,
181 we did not identify potential interactions of Tau with FG-rich Nups, which we had previously
182 reported to interact with Tau[15,38], nor with histones and histone associated proteins[9,37]. We
183 account this to the rather short (10 min) biotinylation reaction time and the potential
184 inaccessibility of Nups in the dense FG-Nup phase of the pore[54]. Interestingly, chromatin
185 associated proteins of the inner NE leaflet (LEM2, EMD, LBR) were not identified as significant
186 interactors of Tau^{P301L}, indicating that oligomerization-prone FTD-mutant Tau may engage less
187 in these intranuclear interactions. LBR was, however, previously found in small cytoplasmic
188 FTD-Tau aggregates[16]. Potential TDP-43ctf interactors clustered in categories associated with
189 the "nuclear outer membrane" and "nuclear envelope", confirming previous results[55].
190
191 ***Brain Tau interacts with nuclear envelope chromatin organizers***
192 The detection of multiple chromatin binding envelope proteins as interactors of Tau was a
193 surprising finding. To verify these interactions, we first performed co-immunoprecipitation (co-
194 IP) assays from nuclear enriched fractions of GFP-Tau expressing cells. At rather harsh salt
195 conditions (~400 mM salt) needed to solubilize proteins out of the nuclear membrane, we could
196 pull-down SUN1 and LBR with GFP-Tau from nuclear lysates (Figure 3A, Supplemental Figure
197 S2A,B).
198 We next tested whether the identified potential Tau interactions would occur at endogenous
199 Tau levels in the cellular environment. Therefore, we applied a series of microscopy-based
200 proximity ligation assays to verify interaction partners of Tau in a semi-quantitative manner. In
201 these assays, the two proteins – Tau and a respective partner protein – are labeled with
202 specific primary antibodies in otherwise untreated, fixed cells or tissue, and their close
203 proximity is detected upon local, spatially restricted signal amplification leading to fluorescent
204 foci at interaction locations (Figure 3B). Using this setup, we first verified the specificity of the
205 assay in human neuronal cells (SH-SY5Y line) using a human Tau specific antibody (Tau13,
206 mouse) alone or in combination with non-binding IgG (rabbit) as negative control (no PLA
207 signal detected), or with another Tau antibody (Tau DAKO, rabbit) as positive control (strong
208 cytoplasmic PLA signal, few PLA spots in the nucleus) (Figure 3C). A combination of antibodies
209 against SUN1 and LaminA/C, interacting at the inner nuclear membrane (INM), was used as
210 a positive control and produced the expected PLA signal restricted to nuclear envelope. Then,
211 we set out to probe the interactions of endogenous Tau with identified NE proteins. After
212 verifying the specificity of each primary antibody by immunofluorescence, we combined them
213 with a Tau antibody and quantified their PLA signal at the NE in comparison to signal produced
214 by the non-binding IgG control. Among the NE transmembrane proteins, we found the LINC
215 complex proteins SYNE2 (Nesprin-2) and SUN1 to produce significant PLA signal with Tau,
216 whereas TMEM43 and NDC1 did not (Figure 3D; Supplemental Figure S2C, S3). Of the INM
217 embedded chromatin binders, Emerin and LBR gave significant PLA signal at the NE (Figure
218 3E). Since we found that Tau can induce heterochromatin alterations (Figure 2), and Tau was
219 previously reported to interact with heterochromatin associated proteins[9,24], we also tested the
220 interactions of Tau with the histone associated proteins HP1α and HP1γ and with the
221 heterochromatin marks H3K9me3 and H4K20me3 (Figure 3F). For these intranuclear proteins
222 we found PLA signal throughout the nucleus, which was significantly enriched over IgG control.
223 This indicated that Tau interacted with additional chromatin-associated proteins that may have

224 escaped the detection by TurboID-Tau proximity biotinylation due to the high stringency of our
225 control condition (TurboID alone) in this assay.
226 We next tested whether the interactions of endogenous Tau with chromatin proteins would
227 occur in neurons. Indeed, PLAs in mature (DIV12) primary hippocampal mouse neurons
228 showed significantly enriched (over IgG control) signal for LEM2, LBR, HP1γ, and HP1α, but
229 not for any of the histone marks tested (Figure 3G; Supplemental Figure S2D,S4). Importantly,
230 PLA of LBR and HP1γ with MAP2, a neuronal microtubule associated protein of constitutive
231 high abundance in the somatodendritic compartment with a domain organization and structure
232 similar to Tau, did not produce PLA signal. This proved that the intranuclear interaction with
233 chromatin binding proteins were specific to Tau. Notably, we could not test Tau/SUN1 or
234 Tau/SYNE2 (Nesprin-2) interactions in primary neurons by PLA because the antibodies used
235 showed unspecific immunodetection and were therefore not suitable to reliably report
236 interactions with Tau.
237 Finally, we investigated whether Tau interactions with chromatin organizing proteins also
238 occurin the human brain. In FFPE-fixed hippocampal AD brain sections, we first verified the
239 specificity of antibody binding for SUN1, LBR, LEM2, and HP1γ by immunofluorescence
240 (Figure 3H, Supplemental Figure S2E), and then performed PLAs in combination with Tau
241 specific antibodies (Tau13 and Tau DAKO) (Figure 3I). To perform conventional
242 immunofluorescence staining for MAP2 and Tau in parallel to PLA on the same brain sections,
243 we modified our standard PLA protocol, allowing us to identify neuronal nuclei (MAP2+ cells)
244 and thereby distinguish between neurons with different levels and states of somatodendritic
245 Tau (i.e., no Tau, diffuse Tau, aggregated Tau in neurofibrillary tangles (NFTs)). For all
246 interaction partners tested (SUN1, LBR, LEM2, and HP1γ), PLA signal occurred inside
247 neuronal nuclei (images recorded for hippocampal area CA1 and molecular layer dentate
248 gyrus), close to the NE, as well as near the nucleolus. For HP1γ, PLA signal was found in
249 areas of DAPI signal across the nucleoplasm. Different negative controls for PLA in human
250 brain, i.e., one antibody alone or nuclear envelope residing SUN1 in combination with
251 postsynaptic PSD-95 that are located far from one another, did not produce PLA signal (Figure
252 3I). Notably, PLA signal for Tau interactions with chromatin associated proteins occurred in
253 neurons with and without diffuse immunolabeling of Tau in the soma, as well as in neurons
254 with aggregated Tau (neurofibrillary tangles, NFTs). This suggests that these interactions
255 occur already at low somatodendritic Tau levels and do not depend on Tau aggregation in the
256 human brain, which matches our observations in primary neurons where soluble endogenous
257 Tau shows the same interactions. In summary, the identified interactions of Tau with chromatin
258 binding proteins at the NE may therefore be part of a physiological Tau function in chromatin
259 regulation.
260
261 ***Tau co-phase separation changes DNA interactions of LBR***
262 We were intrigued by the identification of NE anchored chromatin organizers, i.e., LBR, among
263 the nuclear Tau interactome (Figure 4A), which could be directly related to the observation that
264 Tau overexpression drives DNA close to the NE (Figure 1I). We therefore tested whether Tau
265 would change the interaction of LBR with DNA. When looking at structural characteristics of
266 nuclear Tau interactors, we found that many of them had a predicted high level of protein
267 disorder (PONDR score >0.5) and/or had, like Tau (MAPT), the tendency to form granules
268 (CatGRANULE score >0.75[56]) (Figure 4B). Analysis using PhasePro
269 (http://predict.phasep.pro/[57]) also predicted phase separation propensity for nuclear Tau
270 interactors (Supplemental Figure 5A). A PONDR plot along the amino acid sequence of LBR
271 revealed that its N-terminal regions, which are protruding from the INM into the nuclear lumen
272 and encodes the DNA binding activity, was especially disordered (Figure 4C), suggesting that
273 this domain could be involved in the formation of biomolecular condensates. Hp1γ, which was
274 reported to mediate LBR binding to DNA[54] and form condensates in the presence of DNA[55],
275 showed a disordered region in the middle of its seuquece. Based on these characteristics, we
276 hypothesized that LBR could form condensates and that the presence of Tau may alter the
277 interaction of LBR with DNA based on changing its condensation behavior. To test this idea,
278 we recombinantly produced and purified the LBR N-terminal nuclear projection domain (LBR-

279 npd), Hp1γ, and full-length human Tau (Supplemental Figure 5B) and determined the effect of
280 Tau on LBR-npd phase separation behavior – alone and in combination with DNA – by
281 microscopy. LBR-npd contains a domain for direct DNA binding (aa 1-89) plus a globular II
282 domain (aa 90-211) that mediates the binding of histone-associated HP1 proteins and,
283 thereby, indirectly contributes to DNA[56]. Both domains can be involved in LBR-assisted
284 coordination of DNA at the inner NE. Notably, we used λ-phage DNA (λ-DNA, 47 kbp) covering
285 a wide spectrum of base pair sequences because it is unknown which DNA base pair
286 sequences LBR is binding to.
287 Without DNA, we found that LBR-npd by itself readily forms small circular condensates
288 (diameter 1-2 μm) which assembled into larger grape-like clusters (Figure 4D, left). Tau and
289 HP1γ, or both together, efficiently partitioned into LBR-npd condensates but did not form
290 condensates in the absence of LBR-npd (Figure 4E). Furthermore, FRAP of LBR in
291 condensates showed that Tau and HP1γ cooperatively reduced the LBR-npd molecular
292 mobility inside condensates (Figure 4F), indicating that Tau and HP1γ may independently
293 interact with LBR-npd, possibly at separate binding sites. Next, we added λ-DNA to our
294 experimental setup. Surprisingly, the addition of λ-DNA to LBR-npd, under the same buffer
295 conditions, entirely changed the assembly and appearance of LBR-npd. Instead of forming
296 grape-like condensate assemblies, LBR-npd attached to the added DNA (Figure 5F, right;
297 Supplemental Figure 4C), resulting in thick DNA bundles coated by LBR-npd. We also could
298 observe LBR-npd condensates sitting on and bridging between thinly LBR-npd coated DNA
299 threads. These LBR-ndp assemblies remined of wetting of protein condensates on cytoskeletal
300 fibers, for example, previously described for TPX2 on microtubules[57].
301 In the presence of HP1γ, Tau, or both, LBR-npd still associated with DNA, and HP1γ and Tau
302 colocalized with the larger condensed LBR-npd clusters. FRAP of LBR-npd associated with
303 DNA revealed a mobile molecular fraction of only ~3% (Figure 5L, Supplemental Figure 5D) in
304 all conditions, indicating a tight association of LBR-npd with DNA, regardless of the presence
305 of HP1γ or Tau. To assess whether the presence of Tau could influence the direct interaction
306 between LBR and DNA, we examined the binding of LBR-npd to DNA in EMSA (electrophoretic
307 mobility shift) assays (Figure 4G). Mixing DNA (500 bp fragment; 20 ng = 1 ng/μl) with LBR-
308 npd (400 ng = 20 ng/μl) in the presence of increasing Tau concentrations (0, 25, 50, 75 ng =
309 0, 1.25, 2.5, 3.75 ng/μl) showed that already small amounts of Tau (25 ng) substantially
310 increased the binding of LBR-ndp to DNA (upshift of signal for DNA bound to protein). This
311 strong activity of Tau in enhancing HP1γ-independent binding of LBR-npd to DNA could explain
312 our observation of enhanced chromatin association with the NE in neurons having elevated
313 nuclear Tau. Notably, Tau alone also bound DNA already at very low concentrations, starting
314 at 50 ng/μl (Figure 4G).
315
316 ***Increased somatodendritic Tau is sufficient to induce heterochromatin alterations***
317 Based on previous observations that suggested Tau pathology could modulate neuronal
318 chromatin[10,11], we investigated whether somatodendritic Tau itself would be sufficient to induce
319 changes on the epigenomic level. To investigate the connection between somatodendritic Tau
320 levels and neuronal chromatin organization, we used adeno-associated viruses (AAVs) in
321 cultured hippocampal neurons to overexpress human full-length wild-type Tau (2N4R isoform)
322 or FTD-mutant Tau^{P301L} (Tau o/e, TauP301L o/e), both fused to GFP on their N-terminal end
323 (Figure 2A). Tau^{P301L} has a higher oligomerization and aggregation propensity due to increased
324 accessibility of an aggregation-prone motif (PHF6*; amino acids ^{306}*VQIVYK*^{311}) in the beginning
325 repeat 3 in the Tau repeat domain. Previous studies on Tau's effect on chromatin have been
326 performed in FTD-models expressing similar aggregation-prone Tau variants. Due to its
327 oligomerization, FTD-Tau may engage in different interactions and exert different functions
328 compared to wildtype Tau, which is why we included it in this study.
329 AAV-mediated overexpression of both Tau and Tau^{P301L} induced an overall increase in Tau by
330 ~200% (by Western blot) and in nuclear Tau by ~60% (by immunofluorescence), compared to
331 GFP-expressing control neurons with endogenous Tau levels (Tau base; Figure 5B,C;
332 Supplemental Figure 6A,B). A similar up to 2.5-fold increase in somatodendritic Tau could be

observed for non-aggregated Tau in neurons of Alzheimer's disease brain (Supplemental Figure 6C). To reduce overall Tau levels (Tau k/d), we inhibited endogenous Tau transcription through expression of a *MAPT*-targeted zinc-finger protein array coupled to a gene-silencing KREB transcription factor, ZFP90[28], which reduced overall Tau levels by ~50% and nuclear Tau by ~50% (Figure 5A,B,C). Notably, the Tau knockdown AAV construct expressed equal amounts of ZFP90 and GFP as a transduction marker, separated by a self-cleaving 2a peptide, which allowed for the identification of neurons with reduced Tau levels. The appropriate control, an AAV expressing target-less zinc finger array (ZFP72; Supplemental Figure S6D), did not change cytosolic or nuclear Tau levels compared to GFP expressing or non-treated neurons (Tau base).

To evaluate how the different Tau levels impacted on neuronal chromatin, we investigated the levels and nuclear appearance of classical heterochromatin markers associated with gene repression, H3K9me3 (repressive signal, marks constitutive heterochromatin[30]), and gene activation, H3K9ac (activation mark on enhancers or promotors[32]) and H3K4me3 (activation mark on promotors) (Figure 5D). Compared to GFP expressing control neurons (Tau base), overexpression of Tau (Tau o/e) and mutant Tau^{P301L} (TauP301L o/e) both increased the number of condensed chromocenters (Figure 5E; Supplemental Figure S6E,F) of the repressive H3K9me3 mark. Tau knockdown induced an increase in the chromatin activation mark H3K9ac ($p=0.0064$ by fluorescence intensity). Interestingly, Tau^{P301L} overexpression also increased H3K9ac fluorescence intensity, indicating differential effects of wildtype Tau versus Tau^{P301L} on neuronal chromatin organization. The fluorescence intensity of the other activation mark, H3K4me3, remained unchanged across conditions. The increase in H3K9me3 could be conformed in Tau o/e and TauP301L o/e neurons on the protein level by Western blots of neuronal lysates (Supplemental Figure S6G, S7). Other changes in heterochromatin marks showed the same trend as by fluorescence intensity measurements but remained not-significant by Western bllot.

In summary, increased cytosolic and nuclear wildtype Tau levels appeared to elevate chromatin repression associated with H3K9me3, whereas Tau reduction increased general chromatin activation. This suggests that somatodendritic Tau re-sorting, and corresponding changes in the amount of Tau in and at the nucleus, can influence chromatin repression. Furthermore, aggregation prone FTD-mutant Tau^{P301L} exerted different effects on neuronal heterochromatin than wildtype Tau. This indicates that Tau molecular conformation and oligomerization may play a role in its activity in gene repression.

Tau promotes chromatin association with the nuclear envelope

On top of histone modifications, the spatial organization of interphase chromatin serves as a regulatory level of gene activation and repression. The nuclear envelope plays an important role in this. Chromatin regions associated with the nuclear lamina (lamin-associated domains, LADs) contain mostly repressed genes that can get activated upon dissociation of the LAD from the lamina[34].

In neurons with increased Tau levels we observed a redistribution of DNA in their nuclei. Whereas nuclei of neurons with base-line (untreated and GFP-expressing control neurons) or lower (Tau k/d) Tau levels showed a mostly homogenous distribution (diffuse SiR-DNA or DAPI signal) of DNA outside of chromocenters, nuclei of neurons with elevated Tau levels (Tau o/e and TauP301L o/e) tended to have a higher concentration of DNA (SiR-DNA or DAPI signal) at the nuclear envelope, whereas their nucleoplasm seemed largely void of DNA with few DNA-dense "spots" (Figure 5G,H).

To test whether the enrichment of DNA at the NE in Tau o/e neurons was associated with a physical compaction of DNA, we performed fluorescence lifetime imaging (FLIM) of SiR-DNA labeled DNA in live neurons. SiR-DNA (SiR-Hoechst) is a far-red, fluorogenic, cell permeable live cell DNA probe which can be used to estimate DNA compaction based on its fluorescent lifetime being quenched with increasing DNA density[35]. Using this approach, we found that neurons with high Tau levels (Tau o/e and TauP301L o/e) showed slightly decreased (ns) SiR-DNA lifetimes at the nuclear envelope, indicating that DNA compaction near the NE was mildly increased compared to neurons with baseline Tau levels (Figure 5J,K). Surprisingly, however, Tau o/e neurons showed strongly increased Sir-DNA lifetimes in the core of DNA

chromocenters. The remaining parts of the nucleoplasm were similar to neurons with endogenous or reduced Tau levels. It appeared that chromocenters, normally the regions of highest DNA compaction, became decondensed in their center upon Tau overexpression.

High somatodendritic Tau activates stress response and reduces cholesterol metabolism genes

The identified Tau-related changes in heterochromatin and DNA condensation as well as in LBR interactions with DNA pointed towards a role for nuclear Tau in regulating chromatin organization and gene expression. To examine which genes are responsive to changes in somatodendritic/nuclear Tau levels, we sequenced the total RNA isolated from neurons containing different Tau levels (Tau base, Tau o/e, and Tau k/o; Figure 6A, Supplemental Figure S8A).

Increased somatodendritic/nuclear Tau levels (AAV-induced Tau o/e) induced the significant upregulation (n=87) and down regulation (n=55) of several genes (cut-off: FC>2, adjusted p-value<0.05; Figure 6B,C,D; Supplemental Figure S8B; Supplemental Table T5,T6). Among deregulated genes we find genes that have previously been linked to AD, i.e., upregulation of the lectin-cleaving metalloprotease *Adamts1*, a GWAS risk gene for AD and suggested to improve repair and synaptic plasticity after seizure-induced neuronal damage[58,59], and transcriptions factors *Arid5a* (AT-rich interaction domains 5a), with a function in inflammatory mRNA stability and translation[60] and *Arid5b* involved in metabolic reprogramming and upregulated in amyloid-beta mice[61,62]. Among the downregulated genes are *Hmgsc1* (3-hydroxy-3-methylglutaryl-CoA synthase) that catalyzes an essential step in the cholesterol biosynthesis pathway and is downregulated in AD hippocampus[63], *Neurod6*, a transcription factor important for neurodevelopment and differentiation downregulated AD brain[64], and gastrin-releasing peptide, *Grp*, that stimulates excitatory neurons, likely by binding to GRP receptors on inhibitory neurons and reducing their inhibitory activity[65].

Reduction of Tau (AAV-mediated Tau k/d) had comparably small effects on gene deregulation (significantly up-regulated DEGs (differentially expressed genes): n=2; down-regulated DEGs: n=1 (*Mapt*)). This indicated that increased concentrations of Tau in and around the nucleus, as a consequence of either Tau overexpression or somatodendritic resorting in neuronal stress conditions, could function as signal to initiate gene expression changes.

Gene set enrichment analysis (GSEA; considering all transcriptomic changes; Figure 6E; Supplemental Figures S9A,B,C) indicated that increased Tau levels (Tau o/e vs. Tau base) upregulated pathways of TNFα signaling, apoptosis, and oxidative stress (hypoxia) response. Pathways downregulated by increased Tau levels were mainly involved in cholesterol homeostasis (cholesterol/steroid/lipid biosynthesis and metabolism). GO analysis of the significantly DEGs confirmed that high Tau levels reduced the expression of genes involved in cholesterol, lipid, and Acyl-CoA metabolism as well as voltage gated potassium channels (Figure 6F, top; *GO Molecular function/ Biological Processes;* Supplemental Table T7). In contrast, high Tau levels promoted the expression of genes associated with transcriptional regulation, stress and c-AMP response. Reduction of Tau (Tau k/d vs. Tau base) had little effect on gene regulation and too few genes precluded GSEA and GO analyses. However, Tau reduction increased expression of the transcription factor *Tcfl5* and of vesicle membrane protein *Eqtn* (not significant) involved in membrane fusion and, potentially, endo/exocytosis (https://www.genecards.org/cgi-bin/carddisp.pl?gene=EQTN).

Transcriptional deregulation by Tau involves stress- and AD-related transcription factors

Many of the genes deregulated by high Tau levels where DNA-binding proteins and transcription factors (TFs) that get activated in response to cellular processes stimulated by lipids (*GO Biological Processes*). We were interested, to which extent and how the expression of genes that responded to Tau was coordinated by transcription factors. To predict the transcription factors upstream of Tau-induced expression changes, we performed a wPGSA gene-set analysis[66] using expression data of all genes (except transposable elements, TEs) from Tau o/e and Tau k/d cells. This analysis performs a weighted t-test between sample (Tau o/e or Tau k/d) vs control (Tau base) for each TF included in the analysis. The wPSGA t-score

can be interpreted as the changes in expression of genes regulated by a certain TF. A negative t-score indicates an overall decreased expression of the TF-regulated genes compar7d to control (Figure 6G). TFs with a wPSGA [t score] >+4/<-4 and adjusted p-value $<10^{-5}$ are predicted to be involved in gene deregulation (note, nomenclature from wPGSA analysis used here; TFs shown as gene names; Supplemental Table T8). Interestingly, for both Tau o/e and Tau k/d we found [t score] >4 (compared to Tau base), whereas only six TFs were predicted to have increased downstream expression. This suggests that higher concentrations of Tau might increase the activity or amount of gene repressing factors. Several key TF repressors were upregulated, and their target genes were indeed downregulated in Tau o/e neurons (Figure 6H). For example, (i) by the c-AMP responsive element modulator *CREM*, which regulates metabolic pathways and reactions and is a negative regulator of synaptogenesis in response to neuronal activity[67]. (ii) By the master transcriptional repressor *REST*, which becomes activated in differentiated neurons confronted with ischemic and seizure conditions to protect against neuronal death[68,69], for example, by epigenetically remodeling and repressing the expression of pre- and post-synaptic proteins necessary for neurotransmission[70]. In AD, *REST* and its protective role are downregulated[71,72]. *REST* dysregulation is also implicated in the pathogenesis of epilepsy, Huntington's disease, Parkinson's disease[73–75]. (iii) By *TGIF1*, a TGFβ/Smad induced repressor and regulator of the Wnt pathway that is involved regulating DNA repair and homeostasis[76]. In AD, *TGIF1* is downregulated and Wnt signaling suppressed[77]. The activity of further gene repressing TFs may be regulated by PTMs.

In addition, TFs predicted to respond to higher Tau levels included (i) the immediate early gene *JUNB*, a component of the AP-1 complex that, for example, suppresses metalloproteases in response to neuronal depolarization[78]. In AD, *JUN* was suggested to drive aberrant transposable element mobilization and to be associated with the innate immune response and impair neurogenesis. (ii) The glucocorticoid receptor, *GCR*, which has anti-inflammatory and immunosuppressive functions and is regulated by, as well as controls, AP-1 expression in a negative feed-back loop to regulate stress response[79]. (iii) *BMI1* is a major component of the polycomb group complex 1, that through chromatin remodeling functions as an essential epigenetic repressor of multiple regulatory genes, for example, involved in DNA damage repair, p53 repression and neuronal antioxidative processes[80]. Genes downregulated in response to higher Tau levels could be controlled by histone modifications via histone acetyl transferases (*KAT8, KAT2A, EP300*) and demethylases (*KDM5A, KDM1A, KDM2A*).

Together, these data suggest a complex activity of Tau with the neuronal genome, where the amount of Tau in the somatodendritic compartment and nucleus influences multiple cellular pathways implicated in neuronal physiology as well as inflammatory and cell death pathways observable early in AD brains. Importantly, our data indicate that elevated somatodendritic/ nuclear Tau levels are sufficient to elicit these complex changes in gene activation and repression, multiple of which are deregulated in neurological conditions presenting with somatodendritic Tau re-sorting, i.e., epilepsy and chronic stress[81,82], as well as in AD and other neurodegenerative diseases[83]. This indicates that changes in somatodendritic Tau levels, downstream of different neuronal stimuli, are involved in chromatin organization and transcriptional regulation.

Tau-induced deregulation of lncRNA Neat1 and transposable elements (TEs)

Although the majority of DEGs in Tau o/e and Tau k/d neurons were protein coding genes, we found a few long non-coding RNAs (lncRNAs) to be deregulated as well (Supplemental Figure S9A,D). Among the lncRNAs upregulated in Tau o/e neurons is *Neat1*, an essential component of paraspeckles. *Neat1* is also upregulated in AD brains[84] and has, among other roles, been implicated in decreasing apoptosis in response to metabolic stress[85], cGAS-STING-IRF3 pathway and interferon signaling[86], and regulation of potassium channel activity[87].

CUT&Tag (Cleavage Under Targets & Tagmentation) for the chromatin activation mark H3K9ac, which identifies genomic positions that became more or less activated at different Tau levels, confirmed a strong activation of intronic and non-coding distal intergenic regions in Tau o/e compared to Tau base neurons (Supplemental Figure S10A-C). Further, these data

501 suggested that many activated genome regions associatied with LADs type2 as well as TEs,
502 i.e., LINEs, SINEs, and LTRs, which have previously been linked to Tau pathology[12,13] and
503 spreading[88].
504
505 ***Chromosome and LAD clustering of genes deregulated by Tau***
506 Coordination of gene repression and activation – in addition to histone modifications and
507 transcription factors – is facilitated by associating certain genomic areas with the nuclear
508 lamina[89,90]. These parts of the genome are classified as lamina-associated domains (LADs)
509 and facilitate gene repression through spatial genome organization. LADs of type1 are
510 consistently associated with the nuclear lamina, contain constitutively repressed genes, and
511 contribute to genome stability and cell identity, whereas LADs of type2 are flexible genome
512 regions that are facultative repressive and facilitate dynamic, context-specific gene
513 regulation[91]. Another way of spatial genome organization is provided by nuclear volume
514 territories/domains occupied by individual chromosomes in post-mitotic cells, including
515 neurons[92]. Genes located on the same chromosome are in spatial proximity in a certain
516 volumetric chromosomal territory (CTs).
517 Our DNA and heterochromatin imaging data indicated changes in the spatial organization of
518 DNA in neurons with high Tau levels (Tau o/e), i.e., increased nuclear envelope association
519 and altered chromocenter condensation (Figure 1I,J).To test whether the altered spatial DNA
520 organization would align with changes in gene expression, we determined the chromosomal
521 and LAD association (assignment based on data for midbrain human neurons[93]) of significant
522 DEGs in Tau o/e neurons. Genes deregulated upon increasing Tau levels were distributed
523 throughout chromosomes Chr1-19 and ChrX, with most of them located on Chr1 (16 genes;
524 1.0% of Chr1 genes), Chr2 (13 genes, 0.6 % of Chr2 genes), Chr10 (13 genes; 0.8% of Chr10
525 genes), Chr11 (12 genes; 0.5% of Chr11 genes), Chr13 (10 genes; 1.0% of Chr13 genes), and
526 Chr17 (12 genes; 1.1% of Chr17 genes) (Figure 6I; Supplemental Figure 11A). Interestingly,
527 Chr1, having the most DEGs in Tau o/e neurons, was reported to be associated with the NE
528 and the nucleolus[94], nuclear entities where LAD regions attach.
529 Additionally, we find that >50% of significant DEGs (79 of 142 DEGs) in Tau o/e compared to
530 Tau base neurons were associated with LADs (LAD type1: 22 DEGs = 15% of all DEGs; LAD
531 type2: 57 DEGs = 40% of all DEGs), confirming a pronounced effect of Tau on genes
532 associated with the nuclear envelope (Figure 6J; Supplemental Table T9). LAD type1 assigned
533 DEGs in Tau o/e neurons did not cluster in certain GO pathways but coded, for example, for
534 proteins involved in neuronal activity and metabolism. LAD type2 assigned DEGs clustered
535 significantly in the cholesterol synthesis/metabolism pathway (4 DEGs; GSEA Panther 19.0
536 Reactome) and coded for a number of TFs. In addition, LAD type2, but not type1, DEGs had
537 a significant enrichment in Chr13 and ChrX (Figure 6K,L; Supplemental Figure 11B,C).
538 Comparing Tau o/e with Tau k/d neurons, we find an additional significant association of
539 LADtype2 DEGs with Chr18 (Figure 6L; Supplemental Figure S11C). Notably, Chr13, Chr18,
540 and ChrX have been reported to be located near the nuclear envelope in interphase nuclei of
541 mammalian cells[44,95,96], which is in line with the LAD type2 DEG content we detected in neurons
542 with high Tau levels. Furthermore, ChrX was shown to re-localize from the NE into the nuclear
543 interior in epileptic neurons of human brains[96], a condition that is also linked to somatodendritic
544 Tau re-sorting upon neuronal hyperactivity.
545
546 These findings suggest that high somatodendritic Tau levels alter the expression of DEGs in
547 chromosomes that are located near the NE in interphase and neuronal nuclei. We observe a
548 significant association of Tau induced DEGs, including genes involved in cholesterol
549 biosynthesis and metabolism, with facultative LADs of type2, which represent genomic
550 elements responsive to conditional cellular adaptation. These findings suggest that increased
551 somatodendritic Tau protein levels – as a result of physiological stress or neuronal
552 hyperactivity induced Tau re-distribution – could regulate the cholesterol metabolism and other
553 pathways on the genomic level by interfering with the NE association and condensation of
554 chromatin.
555

Discussion

The neuronal subcellular redistribution and somatodendritic "invasion" of Tau occurs in response to diverse neuronal stimuli, including physiological temperature changes, mechanical stimulation, and glucocorticoid/stress. This suggests that resorting of Tau – and its access to somatodendritic cellular compartments like the nucleus – is part of the physiological neuronal stress-response and encodes general neurophysiological function(s). Understanding the physiological function of Tau resorting is key to deciphering the reason for this frequent event, which also is one of the initial steps in the etiology of multiple neurodegenerative diseases and conditions. Here we show that increasing Tau protein level in the neuronal somatodendritic compartment – to levels comparable to human brain neurons in pre-pathological conditions – is sufficient to induce pronounced changes in chromatin structure and gene expression. Interactions of Tau with nuclear envelope proteins seem to alter the interaction and repression of chromatin at the nuclear lamina.

Elevated Tau levels induce neuronal stress response and metabolic adaptation on the transcriptomic level.

Previous studies suggested that Tau pathology in AD and tauopathies, i.e., the aggregation of non-mutant Tau in human AD brains[11] and the somatodendritic accumulation and aggregation of FTD-mutant Tau in animal models of tauopathies[10,12], is linked to changes in heterochromatin and gene expression. Reported changes included the association of AD Tau pathology with gene activating heterochromatin mark H3K9ac and a reduction of lamin-B, the repressive mark H3K9me2, and histone binding protein HP1α in tauopathy models. Since somatodendritic resorting of Tau is considered to be upstream of Tau aggregation in AD[97], the herein investigated effects of high neuronal Tau levels on chromatin and gene expression should reflect initial phases of Tau pathology in AD as well as the physiological function of Tau resorting in the neuronal response to physiological stimuli.

We find that a ~2-fold increase in the amount of soluble non-mutant Tau, a condition also reached upon non-toxic high neuronal activity in cultured neurons[98] as well as in the human brain, is sufficient to change the heterochromatin landscape in the neuronal nucleus. Therefor, the direction of chromatin changes is, other than previously suggested for AD brains and animal models with Tau aggregation pathology[10], not unilateral (more repression or more activation) but rather complex. Elevated Tau levels increase markers for activated (H3K9ac) as well as repressive (H3K9me3) heterochromatin, induce DNA de-condensation in the center of repressive H3K9me3 chromocenters, and initiate a shift of DNA towards the nuclear periphery. According to these at the first glance opposite effects on the heterochromatin level, Tau appears to induce both up- and down-regulation of genes. Among deregulated genes, we find a number of genes that control transcription (repressors and activators), including the TFs *Rest, Crem*, and *Jun* and the lncRNA *Neat1* that have been implicated in cellular stress response and AD. This indicates that increased Tau levels are involved in regulating gene groups and pathways. Accordingly, previous Tau ChIPseq data indicated genome-wide binding of Tau in coding and non-coding regions (~30% lncRNAs) and suggested a gene repressor role of Tau in neurons under physiological temperature stress[99].

Genes we find to be upregulated by high Tau levels cluster in pathways of neuronal stress response that were previously reported to be altered in AD and other neurodegenerative diseases (e.g., TNFα/NFKB signaling, apoptosis, p53 pathway). In part, however, the effect on these pathways appeared to be opposite in AD brains though, which may reflect the loss-of-function of physiological soluble Tau in modulating these pathways, for example due to pathological Tau aggregation. Interestingly, microglia fed with recombinant wildtype Tau protein present transcriptomic changes clustering in similar pathways[100] indicating that the here observed effects of Tau on gene expression may not necessarily be neuron specific but can also occur in glia cells that take-up released neuronal Tau from the extracellular space (microglia and astrocytes) or that express low levels of Tau (astrocytes and oligodendrocytes). This scenario would offer a path of Tau protein-dependent brain cell communication.

Among the downregulated pathways, Tau's effect on cholesterol biosynthesis stands out. We find three key enzymes in the cholesterol synthesis pathway to be down-regulated at elevated Tau levels, *Nsdhl* (NAD(P)-dependent steroid dehydrogenase-like) as well as *Hmgcs1* (3-Hydroxy-3-Methylglutaryl-CoA Synthase 1, catalyzing condensation of acetyl-CoA and acetoacetyl-CoA to form HMG-CoA) and *Hmgcr* (HMG-CoA reductase) of the mevalonate pathway. This unexpected result provides important new evidence on the direct consequence and, therefore, cellular reason for Tau resorting induced by (patho)physiological stimuli, offering a new angle on Tau biology. Cholesterol is a central component of membrane biology and lipid-based signaling. Downregulation of *Hmgcs1* and *Hmgcr* reflects a cellular strategy to limit unnecessary cholesterol synthesis in response to changing metabolic needs or environmental cues. For example, during periods of energy scarcity, cells shift their focus to conserving energy, e.g., by breaking down stored lipids for energy production and downregulating cholesterol synthesis to prevent the expenditure of energy on the synthesis of non-essential molecules like cholesterol. A neuronal strategy of "saving" energy by reducing cholesterol production would be in line with the observation that neuronal Tau re-sorting occurs in conditions of energy-demanding high neuronal activity[98]. It was shown that a decrease in neuronal cholesterol reduces synaptic activity[101], e.g., synaptic vesicle release[102]. Tau resorting under excitatory stress, followed by Tau-induced reduction in cholesterol biosynthesis, could therefore put a break on excitation to avoid further overexcitation. However, extended cholesterol restriction, i.e., because of pathologically prolonged Tau resorting, could lead to synaptic decline and neurotoxicity in AD and tauopathies[101,103]. In addition, it remains to be evaluated whether Tau plays a role for cholesterol syhthesis in glia cells expressing low levels of Tau, i.e., in astrocytes, the major provider of cholesterol/APOE particles in the adult brain, and in oligodendrocytes providing myelin sheets, the main storage of cholesterol in eth brain[104].

Notably, another important regulator of cell metabolism, *IgfF1* (insulin growth factor-1), is upregulated by high Tau levels, suggesting that Tau may be involved in a global adaptation of the neuronal metabolism. Since increased Tau levels seem sufficient to induce these transcriptional changes, Tau may have a central role in the neuronal metabolic response to these stressors.

Furthermore, the activation of stress response pathways and pro-inflammatory cytokines, such as Tnf-α, both of which we observe in neurons with high Tau levels, can lead to a downregulation of enzymes of biosynthetic pathways, including cholesterol production, as part of an acute-phase response aimed at redirecting resources away from non-essential processes like lipid synthesis. Interestingly, certain stress hormones, like glucocorticoids, that have been shown to reduce cholesterol biosynthesis in response to stress or inflammation, also induce the somatodendritic resorting of Tau. It is next to be tested whether Tau proteins are directly involved in regulating the cholesterol response to neuronal stressors like glucocorticoids.

Pathological conditions presenting with phospho-Tau accumulation and aggregation in neuronal cell bodies often involve repeated or extreme versions of physiological stimuli to induce Tau resorting, for example, neuronal hyperexcitation in seizures as a result of amyloid-beta in AD, mechanical brain damage in traumatic brain injury (TBI) and chronic traumatic encephalitis (CTE). In these scenarios, Tau's function in the neuronal stress response may be exacerbated, e.g., due to prolonged stress exposure and, consequently, Tau re-sorting, or lost, e.g., due to Tau aggregation. Indeed, TF and gene expression changes reported in AD, where Tau aggregates in the cytosol and soluble Tau gets sequestered, appear in part to be opposite to what we observe for neurons with elevated somatodendritic soluble Tau levels. A similar observation has been made by *Klein et al.* in human neurons[11]. We propose that the Tau oligomerization and aggregation in AD brains preclude Tau's gene-regulatory function, which results in the discrepancy in gene expression data between neurons with soluble physiological Tau and AD brains. It was suggested that a loss of physiological nuclear Tau would lead to chromatin relaxation and alter transcription[23,25]. Indeed, our interactomics data now show that oligomerizing FTD-mutant Tau^{P301L} lacks most interactions inside the nucleus, i.e., with chromatin regulating/binding protein, even in its soluble form.

The nuclear envelope plays a central role for Tau related chromatin regulation

Neurons with elevated somatodendritic Tau levels showed nuclear DNA accumulation near the NE with more condensed DNA at the NE. In addition, gene expression changes in these neurons associate with chromosomes located at the nuclear periphery in mammalian cells (Chr1, Chr13, Chr18, and ChrX) and with LADs, which physically attach certain genomic regions to the nuclear lamina, usually for gene repression. This is in line with observations in human brain[11], where Tau-related genomic changes in AD clustered in large genomic segments reflecting spatial chromatin organization nuclear lamina association. Notably, although only very small Tau amounts are detectable in the nucleus, the high affinity to LBR (condensates) and other INM chromatin regulators could ensure specificity in Tau's chromatin regulation activity. Additionally, our PLA studies suggested an interaction of Tau with HP1 proteins. A recent study showed that Tau impacts the binding of HP1α to DNA *in vitro*[24], which - similar to LBR investigated in our study - depends on condensed liquid phase interactions. We do not find evidence that Tau alters the co-condensation and interaction of HP1γ with LBR, but instead increases direct LBR/DNA interactions. We therefore propose that Tau/LBR interactions promote chromatin organization of LAD type2 domains independent of HP1 proteins.

Indeed, we find that Tau-induced transcript changes (both up- and down regulation) are enriched in LAD type2 regions, which associate with lamin type B (Lamin-B). Tau resorting leading to increased nuclear Tau levels could thus promote the repression of genes in LADs type2 by promoting their physical association with LBR. Notably, interactions of Tau with Lamins and LBR have been noticed previously[105] but their association with gene expression changes and chromatin structure have not been further investigated. Among the LAD type2 genes repressed at elevated Tau levels we find key cholesterol synthesis genes (Hmgcr, Hmgcs1 and Nsdhl, on Chr13 and ChrX). This is in line with a function of Tau resorting as regulatory step in neuronal metabolic stress response.

Interestingly, animal models expressing pathological aggregating FTD-Tau variants and AD brains, both of which are characterized by cytosolic Tau accumulation and (potential) loss of nuclear Tau, seem to resemble aspects of laminopathies, such as NE distortions and destabilization [106,107], and show chromatin de-condensation. It remains to be clarified whether this results from a loss of nuclear Tau-facilitated compaction of DNA at the nuclear envelope, e.g., involving LBR. It was, however, shown that DNA condensation at the INM can provide mechanical stability to the NE[108].

In conclusion, we offer a novel function of Tau in physically modulating neuronal chromatin organization, preferentially at the nuclear envelope and involving LBR, to induce stress-related gene expression profiles. Previously identified Tau pathology-associated chromatin changes may result from a loss of this function. These findings propel the understanding of somatodendritic Tau re-sorting common in the physiological as well as pathological neuronal context.

Figures

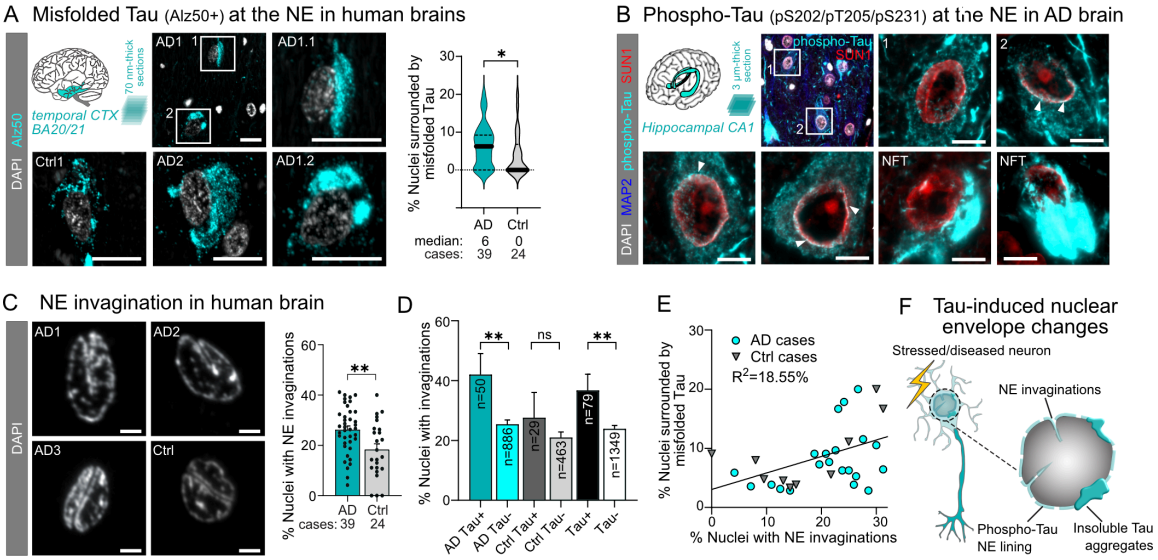

Figure 1. Tau accumulation and nuclear envelope distortion in Alzheimer's disease brains.

(A) Misfolded Tau (Alz50+) near the nucleus in AD (39 cases) and control (24 cases) brain sections (70 nm-thick) of temporal cortex (BA20/21). Data shown as median±quartiles. Student's T-test with Mann-Whithey post-test. Scale bars = 10 µm.

(B) AD and control brain nuclei showing nuclear membrane folds ("invaginations"). Data shown as mean±SEM, one data point per case. Student's T-test with Tukey post-test. Scale bars = 2 µm.

(C) Correlation between the percent of nuclei with nuclear invaginations and with phospho-Tau near the nucleus in AD and control brain sections. Data points present individual cases, linear regression indicated.

(D) Representative images of immunolabeled nuclear envelope protein SUN1 and phospho-Tau (pS202/pT205/pT231) in neurons of AD brains (hippocampal CA1). Neurons with diffuse granular phospho-Tau staining in the soma show phospho-Tau "foci" in proximity to SUN1 in the nuclear envelope (white arrowheads). Tangles (NFTs) do not show this Tau arrangement. Scale bars = 5 µm.

(E) Fraction of neuronal nuclei having invaginations (nuclear membrane folds) in relation to the presence of misfolded/aggregated Tau near the nucleus in AD and control brains (related to Figures 4H,I,J). Data shown as mean±SD, n=number of nuclei as indicated. Two-tailed, unpaired Student's t-test comparing with and without Tau at nucleus within AD and Ctrl groups.

(F) Illustration of nuclear alterations observed in AD brains. Upon somatodendritic Tau re-distribution, phospho-Tau "clusters" appear around the nuclear envelope and insoluble Tau aggregates next to the nucleus, which corelates with nuclear membrane invaginations.

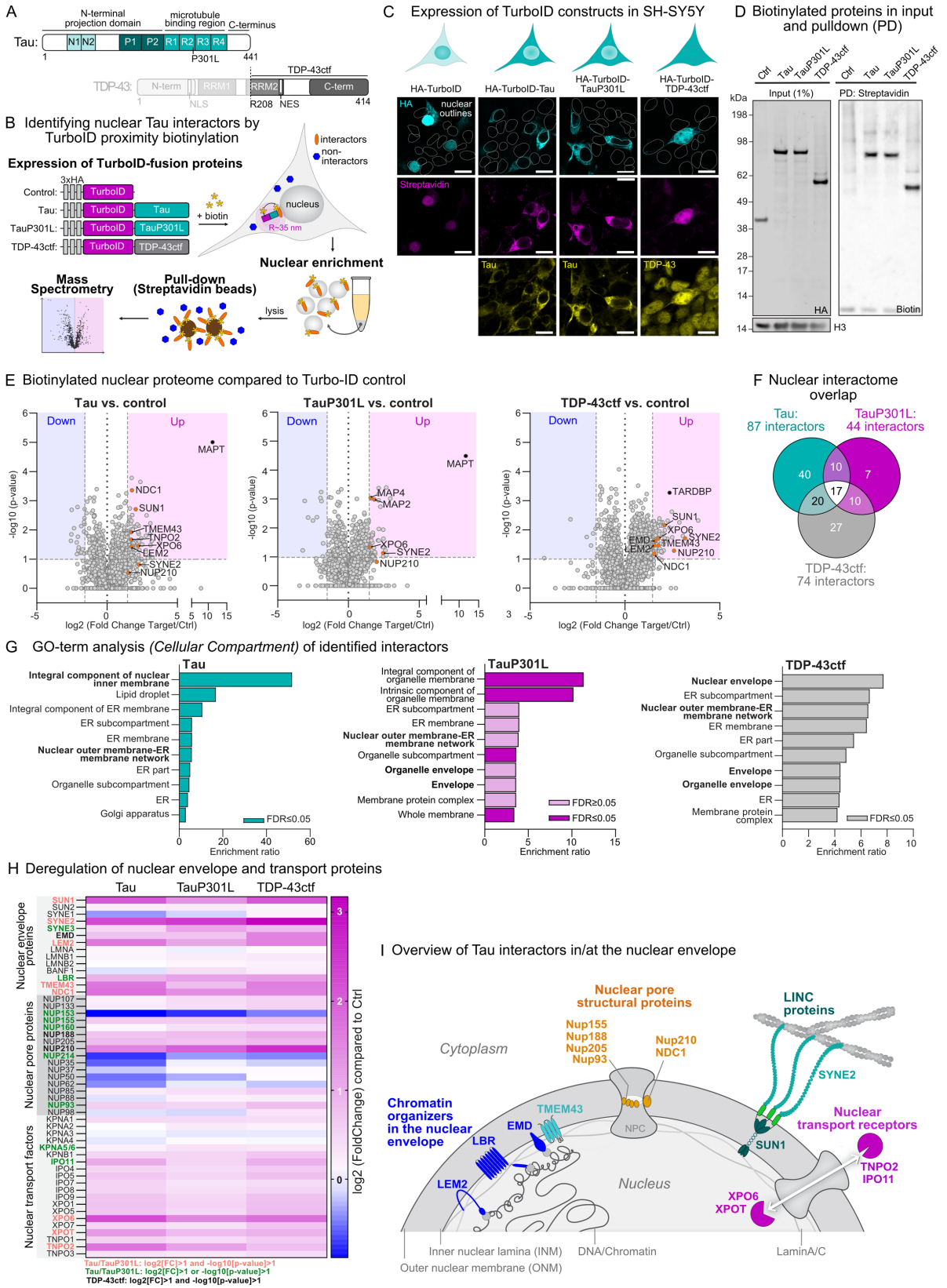

Figure 2. Nuclear Tau interactomics identifies nuclear envelope and nuclear transport proteins.

(A) Domain structures of human wild-type Tau (2N4R isoform) with indicated position of the P301L FTD-mutation in repeat R2, and of human TDP-43 with the location of the C-terminal fragment, TDP-43 ctf, used in this study. Tau domain structures shows positioning of the N-terminal inserts, N1 and N2, and proline-rich regions P1 and P2 in the N-terminal projection domain, the 4 pseudo-repeats R1-R4 in the microtubule-binding domain, and the C-terminus. Full-length TDP-43 is comprised of an N-terminal domain harboring a nuclear localization signal (NLS), two RNA-binding domains (RRM1+2, with a nuclear export signal (NES) in RRM2), and a C-terminal

740 domain. Aggregation-prone TDP-43ctf (C-terminal fragment, aa 208-414) is generated in the brain via auto-
741 cleavage at amino acid R208.
742 (B) Workflow of nucleus-specific proximity biotinylation and identification of proteins associated with HA-TurboID-
743 Tau, HA-TurboID-Tau^{P301L}, HA-TurboID-TDP-43ctf, and HA-TurboID control. TurboID constructs are
744 expressed in SH-SY5Y cells, biotinylation of interacting proteins enabled by addition of biotin to the culture
745 medium. Nuclear interactors are enriched through streptavidin pulldown from nuclear enriched fractions,
746 followed by MS analysis.
747 (C) Expression of TurboID constructs in SH-SY5Y neuroblastoma cells. Anti-HA and staining shows expression
748 and cellular localization of HA-TurboID constructs, successful biotinylation is verified by anti-Streptavidin
749 staining. Tau and TDP-43 staining shows both endogenous and recombinant Tau and TDP-43. White nuclear
750 outlines are derived from DAPI staining. Scale bars = 10 µm.
751 (D) Example western blot of biotinylated proteins in nuclear-enriched cell lysates (input) detected with anti-HA
752 antibody, and in streptavidin beads pulldowns detected with anti-Biotin antibody. Histone-3 (H3) was used as
753 loading control for nuclear fractions/inputs.
754 (E) Volcano plots of mass spectrometry analysis of proximity-biotinylated proteins associated with TurboID-Tau
755 (left), TurboID-Tau^{P301L} (middle), and TurboID-TDP-43ctf (right) each compared to TurboID control. Significant
756 differences in proteins between experimental groups and control were identified using a two-sided t-test. A
757 log2[fold change] >1.5 and p-value < -log10[1] were used as threshold for significance. Selected interactors of
758 interest are indicated as orange data points and labeled with gene/protein identities. Data retrieved from 5
759 biological replicates.
760 (F) Venn diagram showing overlap of significant interactors between Tau, Tau^{P301L}, and TDP-43ctf (created with
761 https://bioinfogp.cnb.csic.es/tools/venny/)
762 (G) Pathway enrichment analysis (ORA, over-representation analysis, Gene ontology (GO), Cellular compartment)
763 for Tau (left), Tau^{P301L} (middle), and TDP-43ctf (right).
764 (H) Heat map representing deregulation of selected nuclear envelope and transport proteins relative to TurboID
765 control.
766 (I) Scheme showing identified Tau and Tau^{P301L} interactors in and at the nuclear envelope. Identified proteins can
767 be categorized as (i) chromatin organizers in the nuclear envelope (LEM2, LBR, EMD), (ii) structural membrane
768 and nuclear pore complex (NPC) proteins (Nup210, NDC1, Nup155, Nup188, Nup205, Nup93), (iii) LINC
769 complex proteins (SUN1, SYNE2), and (iv) nuclear transport receptors (XPO6, XPOT, TNPO2, IPO11).

770

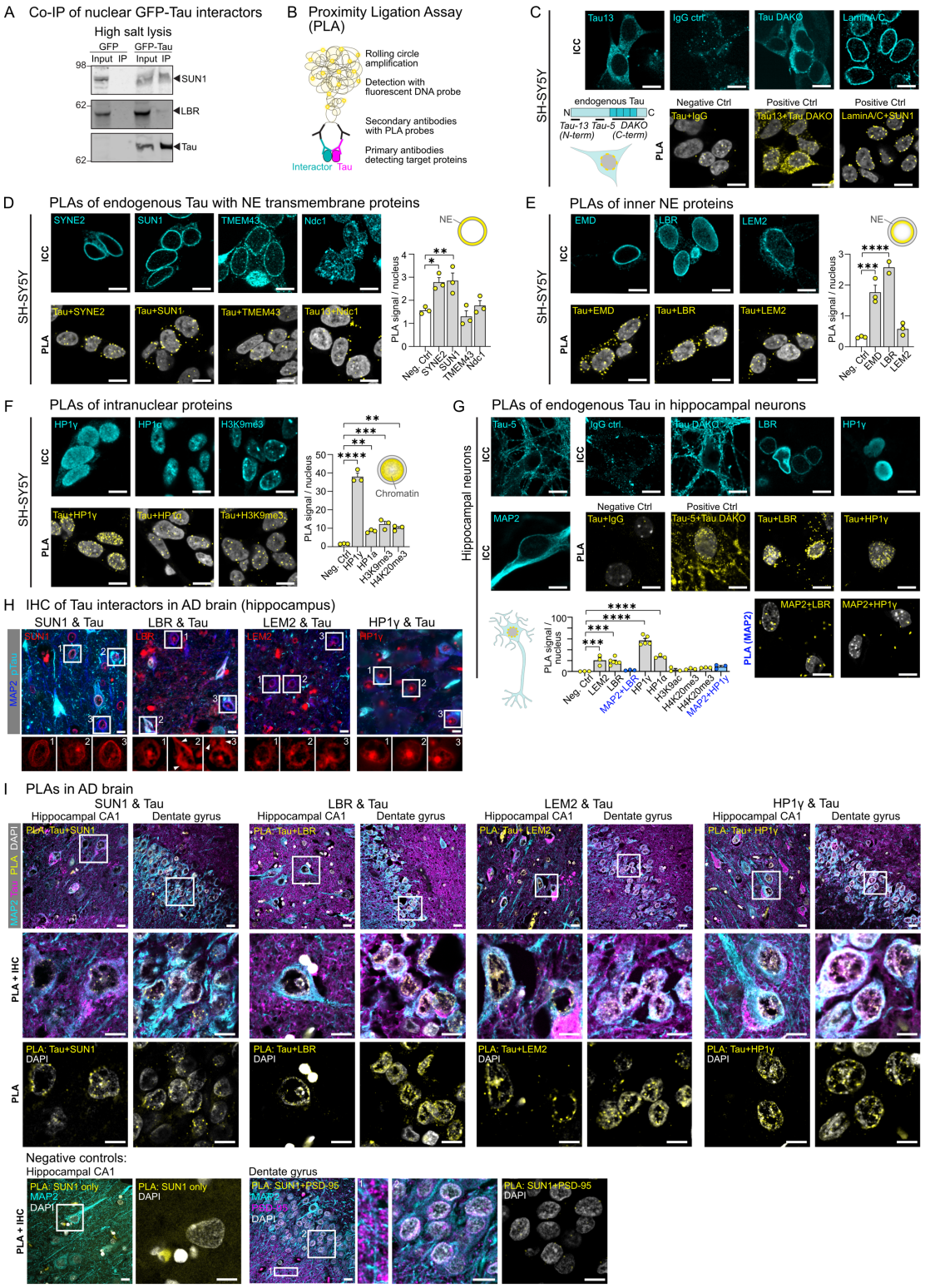

Figure 3. Tau interacts with nuclear envelope chromatin organizers in the brain.

(A) Co-immunoprecipitation of SUN1 and LBR with GFP-Tau in SH-SY5Y cell lysates using high-salt buffer for cell lysis (left).

(B) Principle of proximity ligation assays (PLA) for *in situ* detection of proteins in close proximity (<40 nm).

(C) Positive and negative controls for endogenous Tau PLAs in untransfected SH-SY5Y cells. The negative control (Tau+IgG) shows few unspecific fluorescent PLA signal spots, whereas the Tau positive control using two Tau antibodies (Tau-13+Tau DAKO) results in high PLA signal throughout the cell body. The positive control for nuclear envelope localization, LaminA/C+SUN1, leads to PLA signal around the nucleus. Scale bars = 10 µm.

(D) PLA of endogenous Tau with NE transmembrane proteins in SH-SY5Y cells. Quantification of PLA signal per cell nucleus validate SUN1 and Nesprin-2 as interactors of Tau. PLA signal was quantified in nuclear ROIs. n = 200-400. One-way ANOVA with Dunnett multiple comparison test. Scale bars = 10 µm.

783 (E) PLA of endogenous Tau with inner NE proteins in SH-SY5Y cells. Quantification of PLA signal per nucleus
784 validates Emerin and LBR as interactors of Tau. PLA signal was quantified in nuclear ROIs. n = ~200. One-
785 way ANOVA with Dunnett multiple comparison test. Scale bars = 10 µm.
786 (F) PLA of endogenous Tau with intranuclear proteins in SH-SY5Y cells. Quantification of PLA signal per nucleus
787 validates HP1γ as interactor of Tau. PLA signal was quantified in nuclear ROIs. n = ~300. One-way ANOVA
788 with Dunnett multiple comparison test. Scale bars = 10 µm.
789 (G) PLA of endogenous Tau in mouse hippocampal neurons (DIV12). The negative Control (Tau+IgG) leads to few
790 unspecific fluorescent spots, whereas Tau positive control (Tau-5+Tau DAKO) results in high PLA signal
791 throughout the cell body. PLA signal was quantified in nuclear ROIs. Note that strong neuronal PLA signal is
792 produced for Tau+LBR and Tau+HP1γ, but not for MAP2+LBR and MAP2+HP1γ. n =~50. One-way ANOVA
793 with Dunnett multiple comparison test. Scale bars = 10 µm.
794 (H) Representative images of immunofluorescently labeled Tau interactors (SUN1, LBR, LEM2, HP1γ) in human
795 AD brain sections (SUN1, LBR, HP1γ: hippocampal CA1; LEM2: cortex). Zoom-ins show selected neuronal
796 nuclei/cell bodies (MAP2+) having different phospho-Tau (pS202/pT205/pT231) levels and aggregation states.
797 Note that LBR seems to co-aggregate with phospho-Tau in neurons (arrow heads in zoom-ins). Scale bars =
798 10 µm.
799 (I) Immunostaining for MAP2 (turquoise) and total Tau (pink) in combination with PLAs (yellow) for endogenous
800 total Tau with SUN1 (left column 1), LBR (colum 2), LEM2 (column 3), and HP1γ (right column 4) in human AD
801 brain sections (hippocampal CA1 and dentate gyrus). For each condition, white squares indicate location of
802 zoom-ins shown below for combined IHC+PLA and PLA with DAPI. Bottom: PLA for Human brain negative
803 controls (SUN1 only, SUN1+PSD-95) show no PLA signal. Scale bars = 10 µm.

804

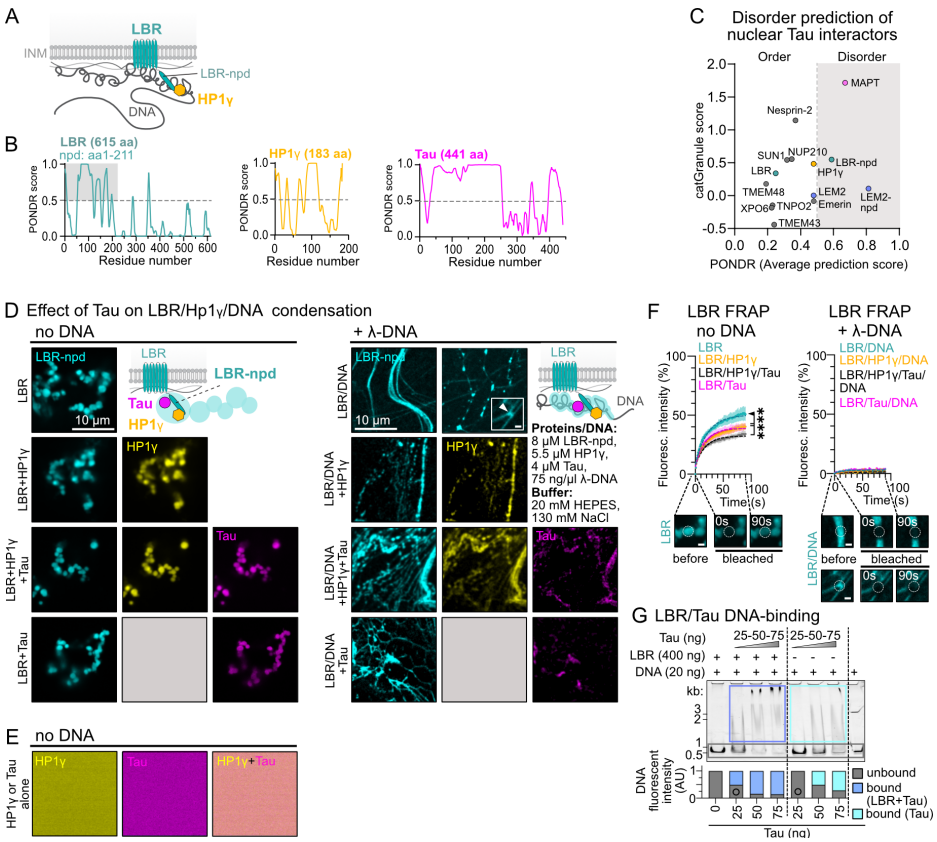

Figure 4. Tau co-phase separation changes DNA interactions of LEM2 and LBR

(A) Schematics of the inner nuclear membrane protein LBR and its direct or HP1γ-mediated interaction with DNA via the N-terminal nuclear projection domain (npd).

(B) Predictions of protein disorder along the peptide sequences of LBR, HP1γ and Tau using PONDR (Predictor of Natural Disordered Regions) reveal disordered regions (PONDR > 0.5) in LBR-npd, in the central region of HP1γ, and the disorder of Tau's N-terminal projection domain.

(C) PONDR vs. CatGranule score (algorithm to predict liquid-liquid phase separation propensity) of identified nuclear Tau interactors shows their disorder (PONDR > 0.5) and/or LLPS propensity (CatGranule > 0.75; http://s.tartaglialab.com/update_submission/902192/d53f367eaf). Note that LEM2-npd has a high disorder/LLPS propensity.

(D) LBR-npd (including 1% LBR-npd-Dylight488) condensation in the presence and absence of HP1γ (including 1% HP1γ-Dylight555), Tau (including 2% Tau-Dylight650), or both under the indicated conditions. Left: in the absence of DNA, LBR-npd readily forms grape-like assemblies of spherical condensates, into which both HP1γ and Tau co-partition. In the presence of λ-DNA (right), LBR-npd attaches to DNA and forms condensates that bundle DNA. HP1γ joins LBR-npd on thin DNA threads as well as in thicker condensates, whereas Tau is only found together with condensed LBR-npd on DNA. Scale bars = 10 µm.

(E) Control conditions showing no condensation of HP1γ, Tau, or both with and without λ-DNA in the used assay buffer conditions. Scale bars = 10 µm.

(F) FRAP of LBR-npd reveals liquid-like recovery in the absence of DNA, whereby HP1γ and Tau reduce the mobile fraction of LBR-npd both independently and co-cooperatively. When bound to λ-DNA, LBR-npd shows almost no recovery regardless of the absence or presence of HP1γ and/or Tau. LBR-npd bound to DNA shows no recovery in any condition. Data shown as mean±SD, n=10-15 condensates per condition from 3 experiments. One-way ANOVA with Tukey post-test was applied to compare the average of the last 10 mean values of each condition. Images show example FRAP images, Scale bars = 1 µm.

(G) Electrophoretic mobility shift assays (EMSA; non-denaturing PAGE on 6% DNA retardation gels) of LBR-npd (400 ng) binding to DNA (500 bp, 20 ng) in the absence and presence (25, 50, or 75 ng Tau) of Tau. DNA was visualized by SYBR® Green EMSA Nucleic Acid Gel Stain. An upshift of signal in the gel lanes indicates that the DNA is bound by added proteins. Quantification of unbound DNA (lower lane parts, grey rectangle) versus LBR-npd/Tau bound DNA (upper lane parts, blue/cyan rectangle) was done based on densitometry. Black circles indicate conditions of comparable LBR-npd concentrations with and without 25 ng Tau.

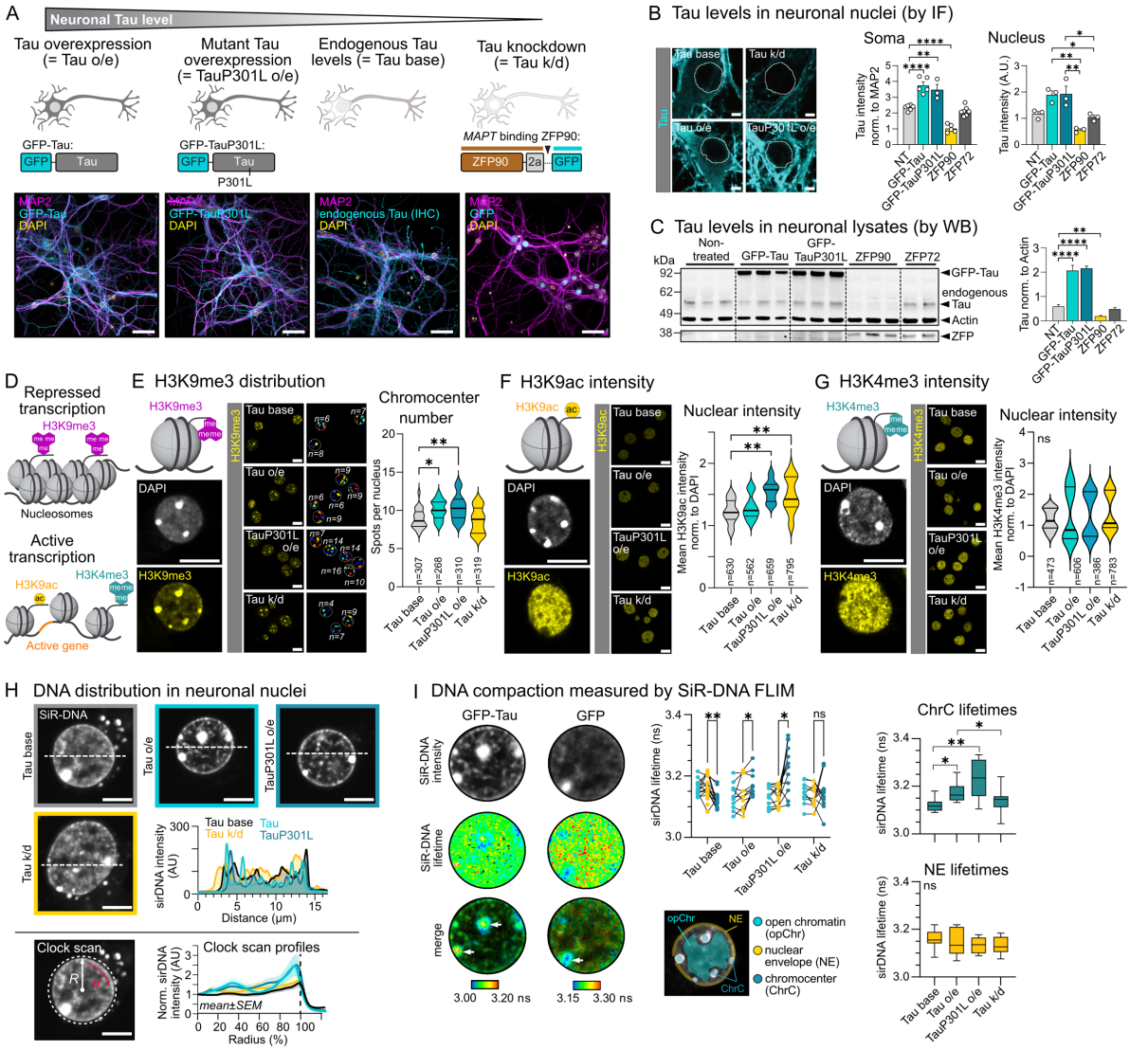

Figure 5. Somatodendritic and nuclear soluble Tau induces heterochromatin alterations.

(A) Modulating Tau levels in primary mouse hippocampal neurons using adeno-associated viruses (AAVs). Overexpression of GFP-tagged human wild-type Tau (2N4R isoform) (Tau o/e) or FTD-mutant Tau^{P301L} (TauP301L o/e) increases Tau levels compared to endogenous mouse Tau (Tau base), whereas the Tau (MAPT) gene silencing zinc-finger protein transcription factor[28] (ZFP90) decreases endogenous Tau levels (Tau k/d). Note that neurons with AAV ZFP90-2a-GFP express GFP due to the 2a self-cleavage site. Images show GFP, immunolabeled MAP2, and DAPI in AAV transduced neurons (DIV12). In untreated neurons (Tau base), endogenous Tau is immunolabeled as well. Scale bars = 50 µm.

(B) Quantification of Tau levels in neuronal somata and nuclei based on fluorescence intensity show modulation of Tau using AAVs from (A). Positions of nuclei, determined from DAPI channel (not shown), are outlined in white. "ZFP72" represents data from non-binding zinc-finger control AAV, ZFP72-2a-GFP (Supplemental Figure S1C). n = 3 images, 50-100 neurons per condition. One-way ANOVA with Dunnett multiple comparison test. Scale bars = 5 µm.

(C) Western blot of neuronal lysates confirms increased Tau levels in Tau o/e and TauP301L o/e neurons and reduced Tau levels in Tau k/d neurons compared to Tau base and ZFP72 control neurons. Glia were removed from cultures by AraC treatment. n = 3 experiments. One-way ANOVA with Dunnett post-test.

(D) Histone modifications associated with gene repression (H3K9me3) and gene activation (H3K9ac, H3K4me3).

(E) H3K9me3 chromocenter number in neurons with different Tau levels. n = number of nuclei (indicated), 3 biological replicates, and 3 images analyzed per condition. One-way ANOVA with Dunnett multiple comparison test. Scale bars = 10 µm.

(F) H3K9ac immunofluorescence intensity in neurons with different Tau levels. n = number of nuclei (indicated), 3 biological replicates, and 3 images analyzed per condition. One-way ANOVA with Dunnett multiple comparison test. Scale bars = 10 µm.

(G) H3K4me3 immunofluorescence intensity in neurons with different Tau levels. n = number of nuclei (indicated), 3 biological replicates, and 3 images analyzed per condition. One-way ANOVA with Dunnett multiple comparison test. Scale bars = 10 µm

(H) DNA (SiR-DNA) distribution in nuclei of neurons with different Tau levels. Representative images (left), line plots (along white dashed lines; middle), and clock scan analyses (n= 5-13 nuclei; right) show DNA enrichment

867 at the nuclear envelope in Tau o/e and TauP301L o/e compared to Tau base and Tau k/d neurons. Scale bars
868 = 5 µm.
869 (I) FLIM of SiR-DNA in neurons with different Tau levels. Compaction/condensation of DNA correlates with a
870 decrease in SiR-DNA lifetime. Representative intensity and lifetime maps of nuclear ROIs are shown for GFP
871 and GFP-Tau expressing neurons. White arrows indicate position of chromocenters. Quantification of most
872 probable SiR-DNA lifetimes was done for different nuclear sub-compartments: Chromocenters (ChrC), open
873 chromatin (opChr), and nuclear envelope (NE). Note that Tau o/e and TauP301L o/e nuclei show an increase
874 in SiR-DNA lifetime in ChrCs. n = 11-17 nuclei per condition from two experiments. Data shown as ChrC, NE,
875 and opChr for individual nuclei (before/after plot; Two-way ANOVA with tukey post-test) and for comparison of
876 ChrC and NE between groups (box-whisker plots, median with 5-95 percentile, one-way ANOVA with Tukey
877 post-test.

878
879

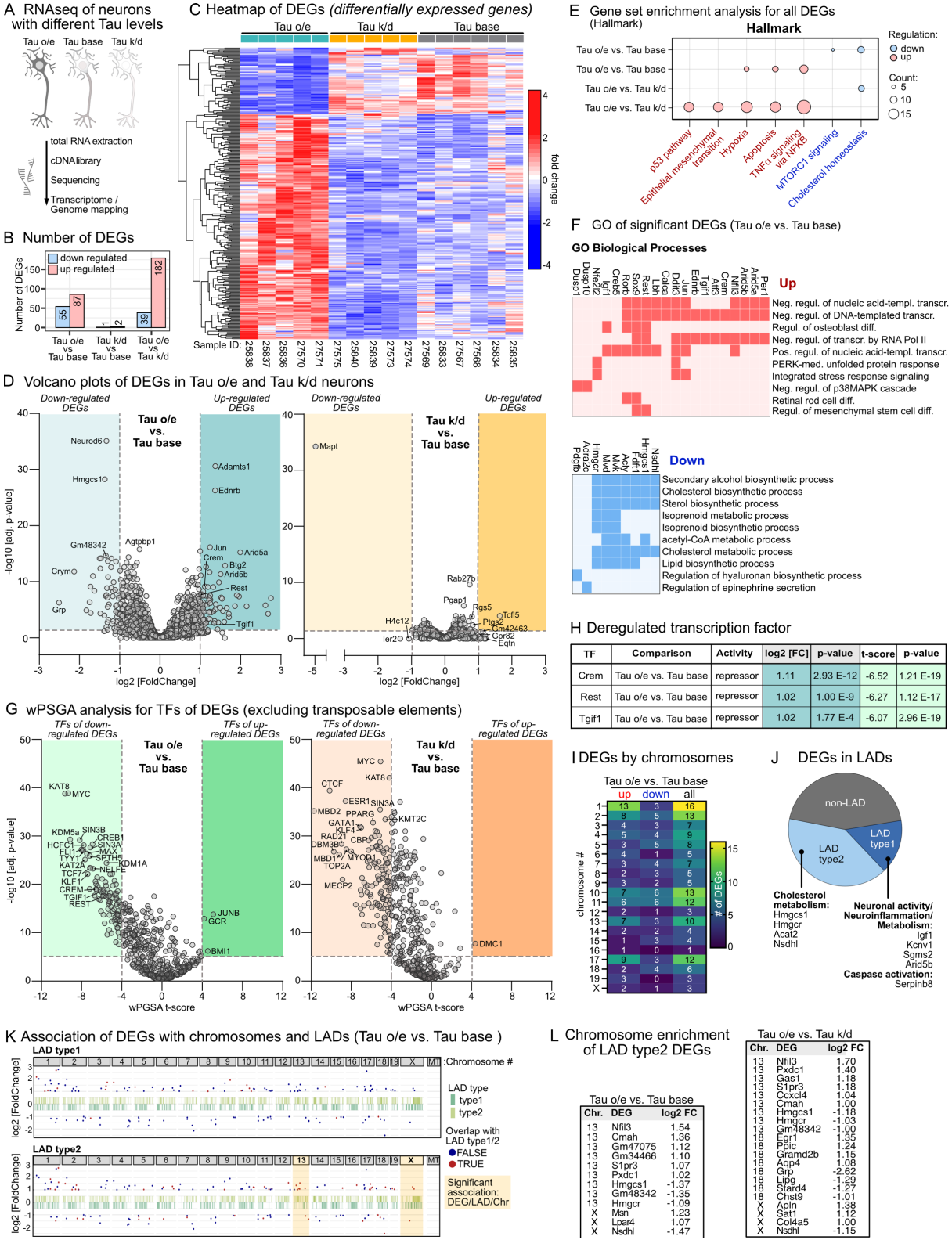

H Deregulated transcription factor

TF	Comparison	Activity	log2 [FC]	p-value	t-score	p-value
Crem	Tau o/e vs. Tau base	repressor	1.11	2.93 E-12	-6.52	1.21 E-19
Rest	Tau o/e vs. Tau base	repressor	1.02	1.00 E-9	-6.27	1.12 E-17
Tgif1	Tau o/e vs. Tau base	repressor	1.02	1.77 E-4	-6.07	2.96 E-19

Tau o/e vs. Tau base

Chr.	DEG	log2 FC
13	Nfil3	1.54
13	Cmah	1.36
13	Gm47075	1.12
13	Gm34466	1.10
13	S1pr3	1.07
13	Pxdc1	1.02
13	Hmgcs1	-1.37
13	Gm48342	-1.35
13	Hmgcr	-1.09
X	Msn	1.23
X	Lpar4	1.07
X	Nsdhl	-1.47

Tau o/e vs. Tau k/d

Chr.	DEG	log2 FC
13	Nfil3	1.70
13	Pxdc1	1.40
13	Gas1	1.18
13	S1pr3	1.18
13	Ccxcl4	1.04
13	Cmah	1.00
13	Hmgcs1	-1.18
13	Hmgcr	-1.03
13	Gm48342	-1.00
18	Egr1	1.35
18	Ppic	1.24
18	Gramd2b	1.15
18	Aqp4	1.08
18	Grp	-2.62
18	Lipg	-1.29
18	Sfard4	-1.27
18	Chst9	-1.01
X	Apln	1.38
X	Sat1	1.12
X	Col4a5	1.00
X	Nsdhl	-1.15

Figure 6. Impact of Tau levels on neuronal transcription

(A) Schematics of RNAseq (total RNA, rRNA depletion) in Tau o/e, Tau base, and Tau k/d neurons.
(B) Number of significant DEGs in Tau o/e and Tau k/d compared to Tau base, and Tau o/e compared to Tau k/d neurons.
(C) Heatmap of significant differentially expressed genes (DEGs) in Tau o/e, Tau k/d and Tau base neurons. Blue: downregulated, red: upregulated DEGs. n= 5-6 neuronal cultures
(D) Volcano plots of DEGs in Tau o/e vs Tau base, and Tau k/d vs Tau base neurons. Threshold of significance was set to log2[FoldChange]>1 and adjusted p-value<0.05. Names of selected genes (mouse) are indicated.
(E) Gene set enrichment "Hallmark" for all DEGs. Up and down-regulated hallmark pathways are shown for Tau o/e vs Tau base, and Tau o/e vs Tau k/d.

(F) Gene ontology (GO *Biological Processes*) of significant DEGs in Tau o/e neurons are shown for up- and down-regulated DEGs.
(G) Transcription factor (TF) analysis (wPGSA) of RNA sequencing data considering all gene expression data except transposable elements. Positive wPSGA t-score of a TF indicates overall upregulation of its target genes, a negative wPSGA t-score an overall down-regulation of the target genes. Threshold of significance was set as [wPSGA t-score] >4 and adjusted p-value $<10^{-5}$. Nomenclature from wPGSA analysis was used.
(H) Selected TFs predicted to have increased gene repressive function in Tau o/e neurons (negative wPSGA t-score), that are found as upregulated DEGs.
(I) Chromosome location of DEGs in Tau o/e compared to Tau base neurons for up- and down-regulated and all DEGs. Number in heat map gives exact number of DEGs in chromosomes spreading across Chr1-19 and ChrX.
(J) LAD association of DEGs in Tau o/e compared to Tau base neurons. Of 142 total DEGs, 22 DEGs (15%) are located in LADs type1 and 57 DEGs (40%) are located in LAD type2. Selected gene names of DEGs for each LAD type are indicated. LAD type2 genes include, for example, cholesterol biosynthesis genes Hmgcr, Hmbcs1, and Nsdhl downregulated in Tau o/e neurons.
(K) Chromosomal distribution of LAD associated DEGs. DEGs in LADs type1 and LAD type2 are distributed across Chr1-19 and ChrX. Significant enrichment of LAD type2 DEGs occurs in chromosomes Chr13 and ChrX for Tau o/e compared to Tau base neurons.
(L) Gene names of DEGs overlapping with LAD type2 and significantly enriched in chromosomes Chr13 and ChrX for Tau o/e versus Tau base neurons, and in chromosomes Chr13, Chr18, and ChrX for Tau o/e versus Tau k/d neurons.

Material and Methods

Human samples

DAPI and Tau imaging: Images of AD and control brain array tomography sections stained for misfolded Tau (Alz50) and DAPI were provided by Prof. Tara Spires-Jones (Centre for Discovery Brain Science, University of Edinburgh). The use of human tissue for these post-mortem studies was reviewed and approved by the Edinburgh Brain Bank ethics committee and the medical research ethics committee. Post-mortem brains of 61- to 96-year-old (24 female, 41 male) AD patients (Braak V-VI, n=40) and healthy controls (n=25) were used (Supplemental Table T10).

IHC and PLA: Post-mortem, FFPE-fixed AD and control brain samples for IHC and PLA were received from the Biobank of the Department of Neuropathology, Charité-Universitätsmedizin Berlin, Germany (Supplemental Table T11). All experiments performed were approved by the local ethics committee at the Charité Berlin, patient consensus to the use of the tissue was given to the biobanks the tissue was received from.

Animals

All experiments involving mice were carried out according to the guidelines stated in the directive 2010/63/EU of the European Parliament on the protection of animals used for scientific purposes and were approved by local authorities in Berlin and the animal welfare committee of the Charité university in Berlin, Germany.

Plasmid constructs

Mammalian expression plasmids encoding for Tau (human full-length wild-type Tau, 2N4R isoform), FTD-mutant Tau^{P301L} (2N4R), and TDP-43ctf (aa208-414) were cloned into 3xHA-TurboID-NLS_pCDNA3 plasmid (Addgene #107171) under a CMV promotor. The TurboID-NLS_pCDNA3 backbone was cut with EcoRI/XhoI to remove the NLS sequence and enable cytoplasmic expression and localization. Tau, Tau^{P301L} or TDP-43ctf inserts were PCR-amplified from different sources (key resource table) and inserted into the backbone using Gibson Assembly cloning. A flexible linker [(SGGG)]3 was inserted between TurboID and the fusion partners to enable correct protein folding. 3xHA-TurboID was cloned from 3xHA-TurboID-NLS_pCDNA3 plasmid (Addgene #107171) using EcoRI to remove the NLS sequence, followed by blunting using T4 polymerase and ligation using T4 ligase. iRFP-Tau (human full-length wild-type Tau, 2N4R) or double mutant $Tau^{P301L/S320F}$ were fused to PCR amplified iRFP670 (Addgene #45466) and insertion into a pRK5-EGFP backbone with CMV

promotor (Addgene #46904) using Gibson Assembly cloning. The Nesprin tension sensor (NesprinTS) was purchased from Addgene (see key resource table).
AAV constructs: Plasmids for GFP, GFP-Tau, GFP-Tau^{P301L}, GFP-p2a-ZFP90, and GFP-p2a-ZFP72 were sub-cloned into an AAV backbone using standard cloning procedures. Genes for ZFP90 and ZFP70 were synthesized based on their published protein sequence[28]. AAV particles (AAV 2/9 PhP.B) were produced by the Charité viral core facility (VCF).

Cell culture and transfection
Human SH-SY5Y cells obtained from ATCC (CRL-2266) were cultured in DMEM (Life Technologies) containing 10% FBS, 1% Pen/Strep (Sigma-Aldrich) and 2 mM L-Glutamine (Thermo Fisher). Cells were grown in 10 cm dishes (60-70% confluency) for proximity biotinylation pulldowns as well as co-immunoprecipitations (co-IPs)/WBs and in µ-slide 8-well imaging dishes (ibidi; ibiTreat) for proximity ligation assays (PLA) and immunofluorescence (IF). Cells were transfected with Lipofectamine 2000 (Life Technologies) according to the manufacturer's protocol.
Human HEK-293 cells obtained from ATCC (CRL-1573) were cultured in DMEM (Life Technologies) containing 5% FBS and 1% Pen/Strep (Sigma-Aldrich). Cells were plated in 35 mm dishes with inserted Coverslip (MaTek) for mechano-compression studies.

Primary hippocampal neurons
Primary neurons were prepared from hippocampi dissected from P0-P1 wildtype mice (C57/B6) of either sex. Hippocampi were dissected in ice-cold HBSS (Millipore) containing 1% P/S. Hippocampal tissue was digested in enzyme solution (DMEM, ThermoFisher Scientific) with 3.3 mM Cystein, 2 mM $CaCl_2$, 1 mM EDTA and papain (20U/ml, Worthington) at 37°C for 30 min. Papain reaction was inhibited by incubating digested hippocampi in DMEM containing 10% FBS (ThermoFisher Scientific), 1% P/S, 38 mM BSA, and 95 mM trypsin inhibitor at 37°C for 5 min. Cells were triturated in complete Neurobasal-A (NBA) medium containing 10% FBS, 2% B-27, 1% Glutamax, 1% penicillin/streptomycin (P/S) and seeded in PLL (0.1 mg/mL) coated glass bottom µ-slide 8-well imaging dishes (ibidi) at a seeding density of ~30'000 cells/cm^2 (for IF/PLA experiments). For Cut&Tag and RNA sequencing experiments, cells were seeded into PLL-coated 6-well dishes (300'000 cells/dish). Every second day, one-fifth of the media was replaced by fresh complete NBA medium.
AraC treatment: To inhibit glial proliferation and obtain mostly neuronal cultures, seeded cells were subjected to a treatment with cytosine arabinoside (AraC) on DIV2. For that, 50% of the medium was removed and kept at 4°C as conditioned medium. Cells were treated with 1 µM (f.c.) AraC for 8 h at 37°C. Then, 80% of the medium containing AraC was removed and conditioned and fresh medium added to obtain the final volume. Success of AraC treatment was exemplary verified by immunostaining with anti-GFAP, anti-MAP2, and anti-Tau antibodies, showing almost full removal of astrocytes without obvious neurotoxicity.
AAV transduction: AAV particles for Tau expression (AAV CAG.EGFP-hTau, AAV CAG.EGFP-hTau^{P301L}), GFP expression (AAV CAG.EGFP), or knockdown of endogenous mouse Tau (AAV hSyn.ZFP90-p2A-EGFP and control AAV hSyn.ZFP72-p2A-EGFP) were added directly into the medium of cultured hippocampal neurons on DIV5, excess particles removed via culture medium change on DIV7, and expression was allowed until DIV12.

Streptavidin pulldown of biotinylated proteins from nuclear-enriched fractions
SH-SY5Y cells seeded in 10 cm dishes were lipotransfected with expression plasmids for 3xHA-TurboID-Tau, 3xHA-TurboID-Tau^{P301L} or 3xHA-TurboID-TDP-43-CTF (10 µg DNA) or 3xHA-TurboID control (5 µg DNA) to achieve similar expression levels. After 15 h, Biotin (50 µM f.c.; Sigma) was added to the medium for 10 min, before cells were washed once with ice-cold phosphate-buffered saline (1xPBS) to stop the biotinylation reaction. Cells were immediately subjected to a cellular fractionation protocol to obtain the nuclear-enriched fraction. For this, cells were scraped in ice-cold hypotonic buffer (250 mM sucrose, 10 mM KCl, 2 mM $CaCl_2$, 1.5 mM $MgCl_2$, 20 mM HEPES pH 7.4; supplemented with protease and phosphatase inhibitors (ThermoFisher Scientific); 0.5 ml/10 cm dish) and kept on ice for 10 min. Cell lysis was achieved by passing the cells four-times through a 25/26-gauge needle

(Omnifix). The crude nuclear fraction (nuclei and some cell debris) was obtained as a pellet from a 1'000 g spin for 5 min. The nuclear pellet was washed once in hypotonic buffer (0.5 ml/sample), passed 5x through a 25/26-gauge and subsequently centrifugated again at 1'000 g for 10 min. After removal of the supernatant, the nuclei pellet was resuspended in 50 µl Urea buffer (8 M urea, 50 mM Tris-HCl pH 7.5; supplemented with 1.25 mM $MgCl_2$ and DNAse-I (ThermoFisher Scientific), and protease and phosphatase inhibitor), mixed for 20 min on a rotating wheel, and sonicated three-times with 2-s pulses. Nuclear lysates were centrifuged at 20'000 g at 4°C for 15 min and the supernatant transferred into a fresh Eppendorf tube. Total protein concentration of nuclear-enriched fractions was measured by BCA assay, and the lysates stored at -80°C until further use.

For the pulldown of biotinylated proteins, streptavidin agarose beads (GE Healthcare) were used in combination with spin columns with inserted 10 µm filter (MoBiTec). Streptavidin-agarose bead slurry (20 µl) was added to each column, washed once with 300 µl PBS, and centrifuged for 1 min at 2'000 rpm. To block unspecific binding, beads were incubated with 300 µl 1% BSA in PBS for 1 h at room temperature under rotation. Meanwhile, all sample protein concentrations were adjusted by dilution in urea buffer to a volume of 400 µl and 1% of input samples was withdrawn and saved for analysis by western blot. For protein pulldown, blocked beads were incubated with nuclear-enriched fractions over night at 4°C under rotation. Columns were centrifuged to separate flow-through from the pulled-down biotinylated proteins, beads were washed 3-times with 300 µl wash buffer (2 M urea buffer) and once with detergent-free PBS. Finally, beads were resuspended in PBS supplemented with protease and phosphatase inhibitor (50 µl/sample). 20% of the samples were used for immunoblotting, the remaining 80% were kept at -20°C until analysis by mass spectrometry. Five independent biological replicates (proteins extracted from five different cell cultures at 5 different days) were performed for mass spectrometry.

Mass spectrometry

In solution tryptic digest: First, proteins in samples were denatured in 8 M urea in 50 mM TEAB, pH 8.5, then samples were reduced with 5 mM DTT at 37°C for 60 min. This was followed by alkylation with 40 mM chloroacetamide at room temperature for 30 min in the dark. Protein digestion was carried out using Lysyl endopeptidase C (Wako) in a first step at an enzyme-to-protein ratio of 1:150 (w/w) at 37°C for 4 h. The sample was diluted using 50 mM TEAB, pH 8.0 to 2 M urea. The second digestion step was performed with trypsin (Serva) at an enzyme-to-protein ratio of 1:100 (w/w) at 37°C overnight. Samples were desalted with C8 material (Waters) in 300 µl pipette tips, dried under vacuum, and stored at -20°C until further use.

LC-MS analysis: LC-MS analysis was performed using an UltiMate 3000 RSLC nano LC system coupled online to an Orbitrap Fusion mass spectrometer (Thermo Fisher Scientific) with instrument software version 3.4. Proteins were separated by an in house packaged 50 cm analytical column (Material: Poroshell 120 EC-C18, 2.7 µm, Agilent Technologies) with 120 min gradients of linearly increasing ACN concentration. Data acquisition for proteomics was performed in positive mode using a MS1(orbitrap)-MS2(ion trap) method. The following parameters were applied: MS1 resolution 120,000; scan range 375 – 1500 m/z; 400k AGC target; 50 ms max. injection time; MS2 scan rate rapid; first mass 110 m/z; 10k AGC target, 35 ms max. injection time; charge state 2-4 enable for MS2; HCD energy 30%; dynamic exclusion duration: 40 s.

Data analysis: LC-MS data were searched using MaxQuant (v.1.6.2.6a) with default parameters against the human proteome (retrieved from Uniprot, 2020, reviewed sequences only). A mass tolerance of 10 ppm was set for precursors on MS1 level, 0.5 Da for fragments on MS2 level. Methionine oxidation and N-terminal acetylation were set as variable, carbamidomethylation of cysteines was set as fixed modification. Proteins were quantified using label free quantification (LFQ) within MaxQuant. Statistical data from five replicates were processed using Perseus (v.1.6.7.0) with default parameters for imputation. For volcano plots and further analysis, a log2-fold change of 1.5 and p-value of 1 were used as threshold for significance. Pathway enrichment analysis was performed using WEB-based Gene Set Analysis Toolkit (https://www.webgestalt.org/) using over-representation (ORA) analysis as enrichment method and geneontology (GO)/cellular component as enrichment categories

(default background). The Venn diagram for the representation of overlapping hits was produced using https://csbg.cnb.csic.es/BioinfoGP/venny.html.

SDS-PAGE and Western blots

Protein samples were mixed with 6x reducing SDS-containing loading buffer, boiled at 95°C for 5 min, and separated by SDS–PAGE (NuPAGE 4-12% Bis-Tris, Invitrogen). Following electrophoresis, proteins were transferred to a nitrocellulose membrane, then the membrane was blocked with 3% BSA in PBS containing 0.05% Tween (PBS-T) at room temperature for 1 h. Membranes were incubated with primary antibodies diluted in blocking solution (PBS-T, 3% BSA), overnight at 4°C, washed 3-times for 5 min in PBS-T, and then incubated with fluorescent dye conjugated secondary antibodies diluted in blocking solution for 1 h at room temperature. Membranes were imaged using a Licor imaging system (Odyssey DLx). A complete list of antibodies used in Western blots can be found in the key resource table.

Co-Immunoprecipitation (co-IP) from nuclear-enriched fraction

SH-SY5Y cells were transfected with EGFP-Tau or EGFP (Addgene #176015) plasmids (10 µg/10 cm dish) using Lipofectamine2000 and allowed to express the constructs for 24 h. The nuclear-enriched fraction was prepared as described above via cellular fractionation with the following changes: i) For Co-IP experiments under high-salt conditions, HEPES buffer (20 mM HEPES pH 7.9, 400 mM NaCl, 1 mM EDTA, and 1 mM EGTA, containing protease/ phosphatase inhibitors) was used to resuspend the final nuclear pellet, followed by sonication 3-times for 3 sec. After nuclei lysis, GFP-trap magnetic particles M-270 (#gtd-20) were used for immunoprecipitation following the manufacturer protocol. In short, 25 µl beads slurry were used per sample and beads were equilibrated once with wash buffer (10 mM Tris/Cl pH 7.5, 150 mM NaCl, 0.05 % NP40, 0.5 mM EDTA; 0.5 ml/sample). For pulldown, nuclear lysates were adjusted to 0.5 ml in dilution Buffer (10 mM Tris/Cl pH 7.5, 150 mM NaCl, 0.5 mM EDTA, containing protease/phosphatase inhibitors) and incubated for 1 h at 4°C under rotation. Flow-through was separated from magnetic beads using a magnet, and beads were washed 3-times with wash Buffer. Protein elution was achieved by resuspending the beads in 80 µl educing 2x SDS sample buffer and boiling at 95°C for 5 min. Supernatants containing proteins were loaded on SDS-PAGE gels.

Immunocytochemistry (ICC) / Immunohistochemistry (IHC)

Cells (SH-SY5Y or primary mouse hippocampal neurons, DIV12) were washed with PBS before fixation with 4% PFA in PBS for 15 min, followed by a wash with TBS for 10 min. After fixation, cells were permeabilized using 0.5% Triton-X100 in PBS for 20 min, blocked with 3% normal goat serum (NGS) in PBS for 1 h at room temperature, and incubated with primary antibodies diluted in 3% NGS/PBS over night at 4°C, or at room temperature for 2 h. After 3x10 min washes in PBS, cells were incubated with secondary antibodies in 3% NGS/PBS for 2 h at room temperature, then washed 3-times in PBS again before nuclei were counterstained with DAPI (1:1000 in PBS) for 15 min.

For IHC of human brain tissue, glass slide-mounted 3 µm-thick formalin-fixed, paraffin-embedded human hippocampus and temporal cortex sections were deparaffinized and baked in citrate buffer for antigen retrieval using Ventana Benchmark GX Staining System according to manufacturer protocol, followed by 3x10 min washes in PBS. Sections were surrounded with a hydrophobic barrier, followed by permeabilization in PBS containing 0.5% Triton-X for 10 min and washing in PBS for 10 min. Sections were blocked at room temperature for 1 h in PBS containing 10% NGS and 0.2% Triton-X100 (150-200 µl/slide). Primary antibodies were diluted in blocking solution and applied to sections overnight at 4°C in a humidity chamber under gentle agitation (100-200 µl/slide, depending on tissue size). After 3x10 min washes in PBS at room temperature, sections were incubated secondary antibodies diluted in 10% NGS and 0.2% Triton-X100 (150-200 µl/slide) for 1 h at room temperature. Finally, tissue auto-fluorescence was reduced by immersing the sections in 0.1% Sudan Black B in 70% ethanol for 20 min at room temperature followed by washing in PBS. The sections were mounted with mounting medium containing DAPI (DAKO). A complete list of antibodies used for ICC/IHC can be found in the key resource table.

1118
1119 *Proximity ligation assays (PLAs)*
1120 PFA fixed cells (SH-SY5Y or primary mouse hippocampal neurons, DIV12) or FPPE human
1121 brain tissue were permeabilized as described above, and subsequently blocked (Cells: 3%
1122 BSA in PBS/0.1% Triton-X100; Tissue: Duolink blocking solution) for 1 h at room temperature.
1123 Proximity ligation assays were performed according to manufacturer protocol
1124 (Duolink®InSituDetection Reagents Red, Sigma-Aldrich). Cells/tissue were incubated with
1125 diluted primary antibodies (Cells: in 3%BSA, 0.1% Triton in PBS, 80µl per sample; Tissue: in
1126 Duolink antibody diluent, 120 µl per sample) for 1 h at 37°C or overnight at 4°C in a humidity
1127 chamber under gentle agitation. Unbound primary antibodies were removed by washing
1128 samples 3-times in wash buffer A (0.01 M Tris, 0.15 M NaCl, 0.05%Tween) under gentle
1129 agitation. Samples were incubated with PLA probes (Duolink®Anti-Rabbit PLUS and Anti-
1130 Mouse MINUS) diluted 1:5 in antibody diluent (80-120 µl/sample) for 1 h at 37°C in a humidity
1131 chamber, then washed 2-times for 5 min in wash buffer A under gentle agitation to remove
1132 unbound PLA probes. For the ligation reaction, samples were incubated with Duolink®Ligation
1133 reagent (Ligation stock 1:5 in antibody diluent plus ligase, 1:40; 80-120 µl/sample) for 30-60min
1134 at 37°C in a humidity chamber, followed by 2x5 min washes with wash buffer A. For signal
1135 amplification, Duolink®Amplification stock was diluted 1:5 in high-purity water, and polymerase
1136 (1:80) was added before slides were incubated in 80-120 µl/sample for 120 min at 37°C in a
1137 humidity chamber. Final washing was performed twice for 10 min in 1X wash buffer B (0.2 M
1138 Tris, 0.1 M NaCl) and once for 1 min 0.01 X wash buffer B. Cells in 8-well chambers were
1139 incubated with DAPI in PBS (1:1000; D9542, Sigma) for 15 min at room temperature. Human
1140 tissue was additionally counterstained after PLA reaction by incubating the sections with
1141 primary antibody diluted in 10% NGS/PBS overnight at 4 °C under gentle agitation, washing
1142 10 min with PBS at room temperature, and incubating with secondary antibody in 10%
1143 NGS/PBS for 1 h at room temperature. To reduce tissue autofluorescence, sections were
1144 immersed in 0.1% Sudan Black B in 70% ethanol for 20 min at room temperature and washed
1145 with PBS. Brain sections were mounted with mounting medium containing DAPI (DAKO). A
1146 complete list of antibodies used for ICC/IHC and PLA can be found in the key resource table.
1147 Imaging of PLAs was performed on a scanning confocal microscope (Nikon Spinning Disk
1148 Confocal CSU-X) using a 60x oil objective.
1149
1150 *Array tomography of human brains*
1151 For high resolution imaging of human nuclei, tissue from inferior temporal gyrus, BA20/21 from
1152 40 AD and 25 control cases was collected at autopsy, fixed for 2 hours in 4% paraform-
1153 aldehyde, dehydrated and embedded in LR white resin[113]. Per case two blocks of tissues from
1154 Brodmann area 20/21 (BA20/21) were cut, stained and imaged as confocal z-stacks, and then
1155 analyzed blinded for case ID and Tau channel. Ribbons of 70 nm ultra-thin sections were cut
1156 on a Leica ultra cut and stained with Alz50 (courtesy Peter Davies) and DAPI. Images were
1157 acquired at 63x magnification on a Zeiss AxioImager and aligned with custom macros
1158 (https://github.com/Spires-Jones-Lab/Array_tomography_analysis_tool). Each stack
1159 contained 12 to 24 planes. For each case, at least three stacks from different sections with and
1160 without NFT pathology were analyzed.
1161
1162 *Recombinant proteins*
1163 All plasmids were verified by Sanger sequencing prior to protein production. Final protein
1164 concentrations were measured by BCA assays (Pierce) and the proteins were stored at
1165 −80°C.
1166 Tau: Human full-length wild-type Tau (2N4R) was expressed in *E. coli* BL21 Star (DE3)
1167 (Invitrogen) and as previously described (Barghorn *et al*, 2005). Protein expression was
1168 induced with 0.5 mM IPTG at OD600 = 0.6 for ~3 h at 37°C. Cells were harvested, resuspended
1169 in lysis buffer (20 mM MES, 1 mM EGTA, 0.2 mM $MgCl_2$, 1 mM PMSF, 5 mM DTT, protease
1170 Inhibitors (Pierce Protease Inhibitor Mini Tablets, EDTA-free) and lysed using a French press.
1171 After initial purification by adding 500 mM NaCl and boiling at 95°C for 20 min, cell debris was
1172 removed by centrifugation (50'000 g, 40 min) and the supernatant was dialyzed against low
1173 salt buffer (Buffer A: 20 mM MES, 50 mM NaCl, 1 mM $MgCl_2$, 1 mM EGTA, 2 mM DTT, 0.1 mM

PMSF, pH 6.8), filtered (0.22 µm membrane filter), run through a cation exchange column (HiTrap SP HP,5 ml, GE Healthcare), and eluted with a high salt buffer (Buffer B: 20 mM MES, 1000 mM NaCl, 1 mM $MgCl_2$, 1 mM EGTA, 2 mM DTT, 0.1 mM PMSF, pH 6.8). Fractions containing Tau were pooled, concentrated using spin column concentrators (Protein concentrators; 10–30 kDa MWCO, Pierce), and run through a size exclusion column (Superose 6 10/300, GE Healthcare). Fractions containing purified monomeric Tau were concentrated as before and buffer exchanged to PBS, 1 mM DTT, pH 7.4.

LBR-npd: For His-tagged LBR-NPD, the nucleoplasmic domain of human Lamin B receptor (LBR-npd; aa 1-211) was codon-optimized, and the gene synthesized by VectorBuilder and provided to us in a pET vector for protein expression (pET.LBR-npd(1-211)-TEV-10xHis). Protein expression (E. coli BL21 Star (DE3) (Invitrogen)) was induced with 0.5 mM IPTG at OD600 = 0.6 for 2 h at 37°C. Cells were harvested (6'000 rpm, 20 min), resuspended in lysis buffer (10 mM Tris-HCL, pH 7.5, 500 mM NaCl, 35 mM Imidazole, 1 mM DTT, protease Inhibitors (Pierce Protease Inhibitor Mini Tablets, EDTA-free) and lyzed using a french press. Afterwards, 10 µl Benzonase and 5 mg Lysozyme (Sigma-Aldrich) was added and incubated for 1 h at 4°C under rotation. After centrifugation (1 h at 35'000 g at 4°C), the supernatant of the lysate was filtered through a 0.22 µm membrane filter and loaded onto a Ni-NTA column (HiTrap, 5 ml, GE Healthcare) using a low imidazole buffer (Buffer 1: 10 mM Tri-HCl, pH 7.5 - 8.0, 500 mM NaCl, 35 mM Imidazole, 1 mM DTT), and eluted with a high imidazole buffer (Buffer 2: with 500 mM Imidazole). Fractions containing the protein were pooled, concentrated using spin column concentrators (Amicon Ultra 15 concentrators; 10kDa MWCO, Millipore), and buffer exchanged, using 25 mM HEPES, 500 mM Nacl, 1 mM DTT as final storage buffer.

HP1γ: GST-tagged HP1γ (Addgene: #24076) was expressed in *E. coli* BL21 Star (DE3) (Invitrogen). Protein expression was induced with 0.5 mM IPTG at OD600 = 0.6 for 2 h at 37°C. Cells were harvested (6'000 rpm, 20min), resuspended in lysis buffer (25 mM HEPES-KOH, pH 7.9, 0.1 mM EDTA, 12.5 mM $MgCl_2$, 20 % glycerol, 0.1 mM KCl, 0.1% NP-40 Alternative (Millipore), 1 mM DTT, protease Inhibitors (Pierce Protease Inhibitor Mini Tablets, EDTA-free) and lysed using a French press. Afterwards, 10 µl Benzonase and 5 mg Lysozyme (Sigma-Aldrich) was added and incubated for 1 h at 4°C under rotation. After centrifugation (1 h, 30'000 g, at 4°C) the supernatant of the lysate was filtered through a 0.22 µm membrane filter. The purification was carried out using Glutathion-Sepharos 4B (GE Healthcare) beads, the supernatant was incubated with the beads overnight at 4°C with end-to-end rotation. After incubation the beads were washed with lysis buffer (25 mM HEPES-KOH, pH 7.9, 0.1 mM EDTA, 12.5 mM $MgCl_2$, 20% glycerol, 0.1 mM KCl, 0.1% NP-40 Alternative (Millipore), 1 mM DTT, protease Inhibitors (Pierce Protease Inhibitor Mini Tablets, EDTA-free) and the protein was eluted using 50 mM Tris, 200 mM NaCl, 20 mM reduced glutathione, 0.3 mM TCEP buffer. Fractions containing the protein were pooled, concentrated using spin column concentrators (Amicon Ultra 15 concentrators; 30 kDa MWCO, Millipore). The GST tag was cleaved off using Glutathion-Sepharos 4B (GE Healthcare) beads and thrombin protease (Sigma-Aldrich). After overnight incubation with protease, the supernatant was run through a size exclusion column (Superose 6 10/300, GE Healthcare) and buffer exchanged, using PBS containing 5% glycerol, 1 mM DTT as final storage buffer.

Fluorescent labeling of proteins

Recombinant proteins were fluorescently labeled using amine-reactive DyLight-NHS ester dyes (Thermo Scientific; Tau: DyLight488/DyLight650; LBR-npd: DyLight650; HP1γ: DyLight550) following manufacturer instructions. The dye was dissolved in DMSO to a final concentration of 10 µg/µl, then added in 5- to 10-fold molar excess to the protein in PBS with 1 mM DTT, and the labeling reaction was performed for 2 h at room temperature at 250 rpm. Excess dye was removed by dialysis (Pur-A-Lyzer Mini Dialysis tubes, Sigma-Aldrich; MWCO 12–14 kDa) against PBS, pH 7.4, 1 mM DTT at 4°C. The labeling degree (amount of dye per molecule protein) was determined by measuring the final protein concentration and correlating it to the maximum absorbance of the attached dye. For calculations see manufacturer instructions.

1230
1231 *Protein condensation assays*
1232 LBR-npd: 8 µM LBR-npd (1% LBP-npd-DyLight561) were imaged alone or in the presence of
1233 5.4 µM HP1γ (containing 1% HP1γ-DyLight650), 4 µM Tau (containing 2% Tau-DyLight488),
1234 and/or 75 ng/µl λ-DNA in 20 mM HEPES, pH 7.4, 130 mM NaCl. Samples (3 µl) were pipetted
1235 onto amine-coated 35-mm dishes (Matek), equipped with ddH_2O-soaked tissue to maintain
1236 humidity, and imaged after 1-2 hours.
1237 LEM2-npd and LBR-npd condensates were imaged after 1-2 hours on a spinning disk confocal
1238 microscope (Nikon Spinning Disk Confocal CSU-X) using a 60x oil immersion objective. In
1239 LBR-npd experiments, DNA was visualized by adding DAPI (1:1000 diluted) to the assay mix.
1240 For FRAP experiments, ROIs inside LEM2-npd condensates were selected and the
1241 fluorescence bleached in the respective channel down to 15-20% of the ROI pre-bleach
1242 intensity. For LBR-npd, FRAP was assessed by bleaching individual condensates in grape-
1243 like condensates assemblies (in the absence of DNA) to 20-30% of their pre-bleach intensity,
1244 or by bleaching LBR-npd on DNA to ~10% pre-bleach intensity.
1245
1246 *Electrophoretic mobility shift assay (EMSA)*
1247 To analyze binding of recombinant LBR-npd and Tau to DNA, electrophoretic mobility shift
1248 assays (EMSAs) were performed using an EMSA Kit (Cat# E33075) following manufacturer
1249 instructions. In brief, 20 ng DNA fragments (500 bp NoLimit DNA fragments Cat#SM1641)
1250 were incubated with recombinant protein at indicated amounts in 20 µl 5x binding buffer (50
1251 mM Tris HCl, pH 7.4, 750 mM KCl, 0.5 mM DTT, 0.5 mM EDTA) for 30 min at 30°C. Samples
1252 were supplemented with 6x EMSA gel-loading solution and separated via non-denaturing
1253 PAGE on 6% DNA retardation gels 0.5x TBE gel running buffer at 110 V for 150 min.
1254 Afterwards, DNA in the gel was stained using SYBR® Green EMSA Nucleic Acid Gel Stain
1255 and visualized using a laser-based Typhoon scanner with parameters and filter sets to
1256 visualize 488 dyes.
1257
1258 *RNA sequencing*
1259 Hippocampal mouse neurons were seeded in PLL-coated 6-well plates, AraC-treated on DIV2,
1260 transduced with AAVs for human Tau expression (AAV EGFP-Tau) and mouse Tau
1261 knockdown (AAV ZFP90.P2a.GFP) on DIV5. On DIV12, cells were washed once with PBS
1262 before they were scraped-off in Trizol (Thermo Fisher). RNA isolation was carried out using a
1263 RNeasy Micro Kit (Qiagen) following the manufacturer's protocol. RNA quantity and integrity
1264 were evaluated using the High Sensitivity RNA assay on the TapeStation 4200 system
1265 (Agilent). For RNA sequencing, mRNA libraries were constructed using the TruSeq Stranded
1266 mRNA Library Prep Kit (Illumina), with 500 ng of total RNA as the input material. Library
1267 quantification was conducted with the Qubit High Sensitivity dsDNA assay, and the size
1268 distribution of library fragments was assessed using the D1000 ScreenTape assay on the
1269 TapeStation 4200 system (Agilent). Sequencing was performed in paired-end mode (75
1270 cycles) on a NovaSeq 6000 system (Illumina) using the NovaSeq S4 v1.5 (200 Cycles)
1271 chemistry. Raw sequencing data were demultiplexed using bcl2fastq2 v2.20. RNA seq was
1272 performed on 2 biological replicates with 4 technical replicates each.
1273 RNA Seq analysis: For RNAseq data, fastq files were aligned to GRCm38 using STAR[114] with
1274 the following settings to maximize repeat mapping (--outFilterMultimapNmax 100, --
1275 winAchnorMultimapNmax 100). The TETranscripts[115] package was used to generate a count
1276 table using gencode.vM25.basic.annotation.gtf and the prepared repeat masker file
1277 mm10_rmsk_TE.gtf (https://labshare.cshl.edu/shares/mhammelllab/www-
1278 data/TEtranscripts/TE_GTF/). The following analysis steps were performed in R (v4.3.0) and
1279 R Studio (v1.4.1717). The count table was re-annotated using biomaRt (v.2.56.1)[116]. Genes
1280 with less than 10 counts in at least 5 samples were excluded from the analysis resulting in
1281 19,214 genes kept in the analysis. Normalization of the count matrix was computed with
1282 R/DESeq2 (v1.40.2)[117] and a variance stabilizing transformation applied using the DESeq2 vst
1283 function at default settings. A batch between experiment days was corrected with limma
1284 (v3.56.2) for the visualizations and included as covariate in the following analysis. Differential
1285 expression analysis based on the DESeq2 package was performed adjusting p-values

1286 according to independent hypothesis weighting from the IHW package (v1.28.0)[118] and
1287 applying apeglm shrinkage from the apeglm package (v1.22.1)[119]. DEGs were defined based
1288 on a fold change threshold >2 and an adjusted p-value threshold of <0.05. A gene set
1289 enrichment analysis (GSEA) was performed with the transformed data as the input using
1290 R/fgsea (v1.26.0)[120], whereby the Gene Ontology (GO)[121,122] and the Molecular Signature
1291 Database (MSigDB)[123,124] Hallmark gene set was used.
1292 Transposable elements (TEs): The technique used for the locus-specific TE analysis is based
1293 on the method established by Schwarz et al.[125], who modified the work process of SalmonTE
1294 (v1.9.0; "SalmonTE*: a modified version for locus-specific expression analysis of transposable
1295 elements."HackMD, 2023. https://hackmd.io/@fgaudilliere/B1nlcJ66o) to count TE on a locus
1296 level instead of on a family level[126]. In brief, a library of TEs was generated from the reference
1297 genome (GRCm38) using RepeatMasker (v4.0.9; http://www.repeatmasker.org) and
1298 transformed to a fasta file format with the *alignToFasta.sh* helper script. Short repeats and N-
1299 rich repeated sequences were excluded, and a salmonTE index was subsequently created.
1300 With the indices locus-specific quantification using the *SalmonTE.py* script was performed.
1301 The DESeq2 analysis was done as above described with the following changes. TEs with fewer
1302 than 16 counts were filtered out, resulting in a final dataset of 212,571 TEs. For DE analysis
1303 the Benjamini-Hochberg method for multiple testing correction and the normal shrinkage
1304 estimator for fold change moderation was applied[127].
1305 LADs: For the LAD association data from mid brain human neurons was used and converted
1306 to mouse[93]. The overlap between DEGs and LADs was tested with R/GenomicRanges
1307 (v1.52.0)[128] and a hyper-geometric test was performed per chromosome followed by a
1308 Benjamini-Hochberg adjustment with R/stats (v4.3.0).
1309 wPGSA analysis: To predict transcription factor (TF) changes upstream of altered gene
1310 expression, wPGSA[66] analysis was performed as previously reported[129]. In brief, normalized
1311 count matrixes generated by R/DESeq2 were used, and count values of each perturbed
1312 sample (Tau o/e or Tau k/d) were normalized to the mean count value of control samples (Tau
1313 base) using R (v4.3.3) and R Studio (v2023.12.1+402). The count matrixes normalized to the
1314 mean control values were imputed into the wPGSA package (v1.1.0) to predict altered TF
1315 activity in the perturbed samples. Significantly altered transcription factors were defined on a
1316 t-value threshold of >4 and an adjusted p-value (FDH) threshold of $<1*10^{-5}$. We looked for TFs
1317 that are included in the DEG list using R.
1318
1319 *Cleavage under targets & tagmentation (CUT&Tag) assay*
1320 For the genome-wide analysis of H3K9ac histone mark in primary mouse neurons the
1321 CUT&Tag-IT assay kit (Active Motif) was used according to manufacturer's instructions.
1322 Hippocampal mouse neurons were seeded in PLL-coated 6-well plates, AraC-treated on DIV2,
1323 transduced with AAVs for human Tau expression (AAV EGFP-Tau) and mouse Tau
1324 knockdown (AAV ZFP90.P2a.GFP) on DIV5. On DIV12 cells were harvested from 6-Wells by
1325 scratching in medium, pooling 3 Wells per condition. Cells were bound to Concavalin A beads,
1326 followed by incubation with 1.5 µg primary antibody (H3K9ac) o/n at 4°C using an orbital mixer.
1327 Following, Guinea Pig Anti-Rabbit secondary antibody was added to bind to primary bound
1328 antibody. The following steps included i) binding of CUT&Tag-IT™Assembled pA-Tn5
1329 Transposomes (protein A fused to Tn5 transposase enzyme that is pre-loaded with sequencing
1330 adpters and binds to secondary antibody), ii) Tagmentation (fragmentation and tagging with
1331 sequencing adaptors) and iii) DNA extraction according to the protocol. PCR amplification was
1332 performed using unique combinations of one i7 Indexed Primer and one i5 Indexed Primer per
1333 condition. The final step to obtain libraries for sequencing contained a clean-up using magnetic
1334 SPRI beads. After library generation, the quality was assessed using Agilent TapeStation,
1335 yielding mostly fragments below 500 bp. Libraries were sequenced in a paired end
1336 configuration using NextSeq2000, 10-15 million reads per sample at the BIH/MDC Genomics
1337 Technology Platform, Berlin.
1338 Analysis: Demultiplexed reads were aligned to GRCm39 using bowtie2[130] with the parameters
1339 --end-to-end --very-sensitive --no-mixed --no-discordant –phred33 -I 10 -X 700, and sorted and
1340 indexed using samtools. Duplicate reads were removed using picard. Read fragments from
1341 aligned reads were prepared using bedtools bamtobed to extract read pairs on the same

1342 chromosome with fragments smaller than 1000bp. Fragment bed files were converted to
1343 bedgraphs suitable for SEACR[131] using bedtools genomecov -bg. SEACR was run on each
1344 prepared bedgraph file with 0.005 (top 0.05%) norm stringent as parameters. Peaks identified
1345 in each sample were merged into a single master peak file. A count matrix of counts from each
1346 sample over all peaks was generated using the getCounts from the chromVAR package[132].
1347 Differential peaks were tested using DESeq2 and annotated with genes and genomic region
1348 using annotatePeak with tss region (-3000, 3000) from the ChIPseeker library. Overlaps with
1349 Repeat elements and T1 and T2 LAD elements were detected using findOverlaps.
1350
1351 *Fluorescence microscopy*
1352 Fluorescent images were acquired with a Nikon scanning Confocal A1Rsi+ microscope with a
1353 DS-Q12 Nikon camera at the Advanced Medical BIOimaging (Ambio) Core Facility at the
1354 Charité, Berlin. To prevent crosstalk among the fluorophores, channels were scanned
1355 sequentially, starting from the highest excitation wavelength to the lowest. Fluorescence
1356 lifetime imaging microscopy (FLIM) of SiR-DNA in primary mouse neurons and NesprinTS in
1357 HEK293 cells was performed using a Leica Stellaris 8-Falcon-STED confocal microscope at
1358 the Systems Biology Imaging core at BIMSB/MDC, Berlin. FRAP for LBR and LEM2
1359 condensates was performed on a Nikon Spinning Disk Confocal CSU-W1 SoRa microscope.
1360 Epifluorescence images of immunolabeled human brain slices were collected on a Keyence
1361 BZ-X system. All images were processed with ImageJ or CellProfiler.
1362

Image modality / Microscope	**Point scanning confocal / Nikon A1Rsi+ microscope**
Illumination /Wavelength Selection	Excitation: DAPI = 405 nm; GFP = 488 nm; mCherry = 561 nm; Cy5 = 647 nm
	Emission filters/Bandwidth: DAPI = 450/50; GFP = 525/50; mCherry = 595/50; Cy5 = 700/75
Optics	Magnification: 20x; Type: Plan Apo; Immersion: Air; NA: 0.8; WD (µm) 1,000
	Magnification: 40x; Type: Plan Fluor; Immersion: Oil; NA: 1.3; WD (µm) 200
	Magnification: 60x; Type: Plan Apo; Immersion: Oil; NA: 1.4; WD (µm) 130
Image modality / Microscope	**Inverted fluorescence-phase contast microscope / Keyence BZ-X800**
Illumination /Wavelength Selection	Excitation: DAPI = 360/40 nm; GFP = 470/40 nm; TRITC = 545/25 nm; Cy5 = 620/60 nm
	Emission filters/Bandwidth: DAPI = 460/50; GFP = 525/50; TRITC = 605/70; Cy5 = 700/75
Optics	Magnification: 60x; Type: Plan Apo; Immersion: Oil; NA: 1.40; WD (µm): 130
Image modality / Microscope	**Confocal Leica SP8 Stellaris**
Illumination /Wavelength Selection	Excitation: CFP = 450 nm; GFP = 480 nm; YFP/Venus = 510 nm; iRFP/SirDNA = 645 nm
Optics	Emission filters/Bandwidth: CFP/TFP1 = 500/50; GFP = 525/50; YFP/Venus = 555/50; iRFP/SirDNA = 700/75
Sample Preparation	
	8-well imaging dishes (ibiTreat; Polymer coverslip No. 1.5H)
	8-well glass bottom imaging dishes (Glass coverslip No. 1.5H)
	35 mm dishes (Glass coverslip No. 1.5H)
Specific information	
Transmitted light images (phase contrast, brightfield, DIC)	Figure S7A,B
Multidimensional acquisitions	Figure 1A: 40x stacks, Z-step = 1.5 µm
Live cell imaging	Figure 1I,J; Figure 4B,E; Figure S7A,B

1363

Image analysis

Heterochromatin markers: An image analysis pipeline was created in CellProfiler to analyze heterochromatin intensity and chromocenter number and size. The pipeline for nuclear intensity consisted of: IdentifyPrimaryObjects (in DAPI channel) > MeasureObjectIntensity (in DAPI and HC channel) > MeasureObjectSizeShape. The pipeline for chromocenter analysis consisted of: IdentifyPrimaryObjects (in DAPI channel) > EnhanceOrSuppressFeatures (Enhance: HC in heterochromatin channel) > MasImage > IdentifyPrimaryObjects > MeasureObjectSizeShape > MeasureObjectIntensityDistribution (Bin =4). > RelateObjects

Line plots: Define horizontal line of same length as ROI; ImageJ > Analyze > Plot profile.

Clock scan: The average radial distribution of chromatin in neuronal nuclei was analyzed in SiR-DNA images collected from living neurons. The *Clock scan* plugin of ImageJ was used, which (i) measures the fluorescence intensity profile along a line (radial line) from the center to the outer boundary of an ROI, and (ii) creates an average of all 360 intensity profiles measured upon 360° rotation of the radial line. The output is a graph presenting average fluorescence intensity (y-axis) over the distance to the center in % of radius (x-axis; 100% = nuclear border). Clock scans of nuclei with DNA accumulation is at the NE produce a graph with a peak at ~90-100% radius.

Nuclear invaginations: Z-stacks of DAPI-stained nuclei in AD brain were. Nuclei were identified as “invaginated“ when at least one membrane fold (=invagination) was spotted across the z-stack. The presence of misfolded Tau (Alz50+) around nuclei was determined afterwards by merging DAPI and ALZ50 channels.

TurboID constructs: In representative confocal images (60x) of TurboID constructs expressed in SH-SY5Y cells, nuclei were outlined using the DAPI channel and added as white outlines using *Flatten* in ROI Manager.

PLAs: To quantify PLA signals, nuclei ROIs were defined by thresholding images in the DAPI channel (ImageJ) and defining them as individual particles. Afterwards, PLA signal spots within nuclear ROIs were detected in the PLA channel (Cy3) using the *Find maxima* function. The number of PLA signal spots were normalized to the number of cell nuclei. 2-3 experiments were performed for each condition, and 3-6 images analyzed per condition.

Protein condensates: Surface coverage was determined on an image-by-image base by measuring the area covered by condensates after thresholding the image to remove surface background in ImageJ. Co-partitioning coefficients (= $c_{dense\ phase}/c_{light\ phase}$) were determined on an image-by-image base by dividing the mean fluorescence intensities measured inside condensates by the one measured outside of condensates. Coefficient variance of DNA inside condensates was determined on a condensate-by-condensate base by dividing the standard deviation by the mean of individual condensates (CoeffVar = SD/mean). Line Plots: Lines of same length were drawn across condensates in the LEM2 channel using ImageJ, and the intensity profiles for all channels along the same line measured by the plot profile function. The y-values for each channel were normalized to min=0 and max=1 and plotted in GraphPad Prism 10.

Statistical analysis

For the Statistical analysis GraphPad Prism versions 9 and 10 (GraphPad Software, San Diego, CA, USA; www.graphpad.com) were used. For comparison of two groups, unpaired two-tailed Student’s t-tests were used. For comparison of multiple groups, one-way ANOVAs with Tukey post-test (comparison between all means) or Dunnett post-test (comparison to mean of control) were applied. Significance is indicated as *$p<0.05$, **$p<0.01$, ***$p<0.001$, ****$p<0.0001$.

Data Availability

Mass spectrometry: Proteomics data have been deposited to the ProteomeXchange Consortium via the PRIDE partner repository with the dataset identifier PXD058565 (Reviewer access details**:** Username: reviewer_pxd058565@ebi.ac.uk; Password**:** yPkItu6tXRW5).

Seqiencing data: The bulkRNAseq and Cut&Tag data are available under the following GEO accession number: GSE283514.

Contributions

L.D. and S.W. conceived the project, conceptualized the study, curated data, designed figures, and wrote the manuscript.
L.D. and R.P-L. designed and performed experiments and interpreted data.
S.W. conducted FLIM experiments and analysis.
L.R. and S.W. conducted LLPS experiments and analysis.
C.K. and C.B. performed PLA experiments.
B.A. developed AAV and TurboID vectors
T.K. developed experimental protocols and tools for TurboID experiments.
C.W. performed Mass Spectrometry.
K.S. and P.G. performed RNA-Seq data analysis.
K.T. analyzed human array tomography images.
R.A., A.D.-B., S.H., S.M., B.K.N-H., R.S., M.F. assisted with experiments.
H.R. supplied human brain tissue for PLA and IHC analysis.
T.S.-J. supplied array tomography images from human brain tissue.
E.DeD. and M.B. performed RNA-Seq.
A.N. consulted in RNA-Seq and CUT&Tag experiments and analyzed CUT&Tag data.
T.U. discussed data and reviewed manuscript.
F.L. contributed to discussing the MS data.
A.v.A. provided LEM2 protein, discussed data, reviewed manuscript.
T.T. discussed data and reviewed manuscript.
All authors reviewed and approved the manuscript.

Acknowledgements

We thank Britta Eickholt, Charité Berlin, for enabling the use of Charité department equipment and general support, Carmelo Ferrai, University Göttingen, for data discussions and advise on chromatin imaging, Gabriele Kaminski Schierle, University Cambridge, for advice on SiR-DNA FLIM, Francsico Garciá-Sierra, Cinvestav Mexico City, for sharing protocols for immunofluorescence in human brain tissue, Donato Di Monte and his team, DZNE Bonn, for sharing protocols for PLA in brain tissue, and Paolo Salomoni, DZNE Bonn, for TE data discussion. We thank Thorsten Trimbuch and the Charité viral core facility for AAV vectors production, the Charité Bioimaging core (Ambio) for support in confocal microscopy, Robert Zinzen, MDC BIMSB, for support in FLIM and STED imaging, the single cell sequencing core PRECISE in Bonn, for RNA sequencing and data analysis, the Core Facility Genomics, Berlin Institute of Health at Charité (BIH), for CUT&Tag sequencing, and Max Ruwolt for help with the MS data upload. The authors are most grateful to the individuals and their relatives for consenting to autopsy and subsequent research, which were facilitated by the Biobank of the Department of Neuropathology, Charité-Universitätsmedizin Berlin.

Funding

Funding for this study was granted to S.W. by the BrightFocus Foundation (A2021044S), the Verum Foundation, the Rainwater Foundation, the German Research Foundation (DFG, SPP2191, 506373047), the European Union (ERC 101126140) and the Helmholtz Association. B.A. and L.R. were supported by the Einstein Foundation. TS-J received funding for this collaboration from the UK Dementia Research Institute (award number UK DRI-4004) through UK DRI Ltd, principally funded by the UK Medical Research Council. T.T and K.S received funding by the European Union (ERC, 804468) and DFG (SPP2202, TO 1347/5-1). F.L. and C.W. received funding by the European Union (ERC 949184).

Declaration of interests

F.L. is a shareholder and advisory board member of Absea Biotechnology Ltd and VantAI.

References

1. Parra Bravo, C., Naguib, S.A., and Gan, L. (2024). Cellular and pathological functions of tau. Nature Reviews Molecular Cell Biology 2024 25:11 *25*, 845–864. https://doi.org/10.1038/s41580-024-00753-9.
2. Sultan, A., Nesslany, F., Violet, M., Bégard, S., Loyens, A., Talahari, S., Mansuroglu, Z., Marzin, D., Sergeant, N., Humez, S., et al. (2011). Nuclear Tau, a key player in neuronal DNA protection. Journal of Biological Chemistry *286*, 4566–4575. https://doi.org/10.1074/jbc.M110.199976.
3. Schneeweis, A., Hillyer, D., Lama, T., Kim, D., Palka, C., Djemil, S., Abdel-Ghani, M., Mandella, K., Zhu, W., Alvarez, N., et al. (2024). Mass spectrometry identifies tau C-terminal phosphorylation cluster during neuronal hyperexcitation. J Neurochem. https://doi.org/10.1111/JNC.16221.
4. Braun, N.J., Yao, K.R., Alford, P.W., and Liao, D. (2020). Mechanical injuries of neurons induce tau mislocalization to dendritic spines and tau-dependent synaptic dysfunction. Proc Natl Acad Sci U S A *117*, 29069–29079. https://doi.org/10.1073/PNAS.2008306117/SUPPL_FILE/PNAS.2008306117.SAPP.PDF.
5. Spillantini, M.G., and Goedert, M. (2013). Tau pathology and neurodegeneration. Lancet Neurol *12*, 609–622. https://doi.org/10.1016/S1474-4422(13)70090-5.
6. Chang, C.W., Shao, E., and Mucke, L. (2021). Tau: Enabler of diverse brain disorders and target of rapidly evolving therapeutic strategies. Science (1979) *371*, eabb8255. https://doi.org/10.1126/science.abb8255.
7. Sotiropoulos, I., Galas, M.C., Silva, J.M., Skoulakis, E., Wegmann, S., Maina, M.B., Blum, D., Sayas, C.L., Mandelkow, E.M., Mandelkow, E., et al. (2017). Atypical, non-standard functions of the microtubule associated Tau protein. Acta Neuropathol Commun *5*, 91. https://doi.org/10.1186/S40478-017-0489-6.
8. Kent, S.A., Spires-Jones, T.L., and Durrant, C.S. (2020). The physiological roles of tau and Aβ: implications for Alzheimer's disease pathology and therapeutics. Acta Neuropathol *140*, 417–447. https://doi.org/10.1007/S00401-020-02196-W.
9. Rico, T., Gilles, M., Chauderlier, A., Comptdaer, T., Magnez, R., Chwastyniak, M., Drobecq, H., Pinet, F., Thuru, X., Buée, L., et al. (2018). Tau Stabilizes Chromatin Compaction. Front Cell Dev Biol *9*, 228–239. https://doi.org/10.3389/fcell.2021.740550.
10. Frost, B., Hemberg, M., Lewis, J., and Feany, M.B. (2014). Tau promotes neurodegeneration through global chromatin relaxation. Nature Neuroscience 2014 17:3 *17*, 357–366. https://doi.org/10.1038/nn.3639.
11. Klein, H.U., McCabe, C., Gjoneska, E., Sullivan, S.E., Kaskow, B.J., Tang, A., Smith, R. V., Xu, J., Pfenning, A.R., Bernstein, B.E., et al. (2019). Epigenome-wide study uncovers large-scale changes in histone acetylation driven by tau pathology in aging and Alzheimer's human brains. Nat Neurosci *22*, 37–46. https://doi.org/10.1038/s41593-018-0291-1.
12. Ramirez, P., Zuniga, G., Sun, W., Beckmann, A., Ochoa, E., DeVos, S.L., Hyman, B., Chiu, G., Roy, E.R., Cao, W., et al. (2022). Pathogenic tau accelerates aging-associated activation of transposable elements in the mouse central nervous system. Prog Neurobiol *208*. https://doi.org/10.1016/J.PNEUROBIO.2021.102181.
13. Guo, C., Jeong, H.H., Hsieh, Y.C., Klein, H.U., Bennett, D.A., De Jager, P.L., Liu, Z., and Shulman, J.M. (2018). Tau Activates Transposable Elements in Alzheimer's Disease. Cell Rep *23*, 2874–2880. https://doi.org/10.1016/J.CELREP.2018.05.004.
14. Musi, N., Valentine, J.M., Sickora, K.R., Baeuerle, E., Thompson, C.S., Shen, Q., and Orr, M.E. (2018). Tau protein aggregation is associated with cellular senescence in the brain. Aging Cell *17*. https://doi.org/10.1111/ACEL.12840.
15. Diez, L., Kapinos, L.E., Hochmair, J., Huebschmann, S., Dominguez-Baquero, A., Vogt, A., Rankovic, M., Zweckstetter, M., Lim, R.Y.H., and Wegmann, S. (2022). Phosphorylation but Not Oligomerization Drives the Accumulation of Tau with Nucleoporin Nup98. Int J Mol Sci *23*, 3495. https://doi.org/10.3390/IJMS23073495/S1.
16. Jiang, L., Lin, W., Zhang, C., Ash, P.E.A., Verma, M., Kwan, J., van Vliet, E., Yang, Z., Cruz, A.L., Boudeau, S., et al. (2021). Interaction of tau with HNRNPA2B1 and N6-methyladenosine RNA mediates the progression of tauopathy. Mol Cell *81*, 4209-4227.e12. https://doi.org/10.1016/J.MOLCEL.2021.07.038/ATTACHMENT/300C5D78-3305-4A82-9509-F2A7AF4105BE/MMC13.PDF.
17. Kang, S.G., Han, Z.Z., Daude, N., McNamara, E., Wohlgemuth, S., Molina-Porcel, L., Safar, J.G., Mok, S.A., and Westaway, D. (2021). Pathologic tau conformer ensembles induce dynamic, liquid-liquid phase separation events at the nuclear envelope. BMC Biol *19*, 1–21. https://doi.org/10.1186/S12915-021-01132-Y/TABLES/1.

18. Hochmair, J., Exner, C., Franck, M., Dominguez-Baquero, A., Diez, L., Brognaro, H., Kraushar, M.L., Mielke, T., Radbruch, H., Kaniyappan, S., et al. (2022). Molecular crowding and RNA synergize to promote phase separation, microtubule interaction, and seeding of Tau condensates. EMBO J *41*. https://doi.org/10.15252/EMBJ.2021108882/SUPPL_FILE/EMBJ2021108882-SUP-0002-MOVIEEV1.ZIP.
19. Eftekharzadeh, B., Daigle, J.G., Kapinos, L.E., Coyne, A., Schiantarelli, J., Carlomagno, Y., Cook, C., Miller, S.J., Dujardin, S., Amaral, A.S., et al. (2018). Tau Protein Disrupts Nucleocytoplasmic Transport in Alzheimer's Disease. Neuron. https://doi.org/10.1016/j.neuron.2018.07.039.
20. Maina, M.B., Bailey, L.J., Wagih, S., Biasetti, L., Pollack, S.J., Quinn, J.P., Thorpe, J.R., Doherty, A.J., and Serpell, L.C. (2018). The involvement of tau in nucleolar transcription and the stress response. Acta Neuropathol Commun *6*, 1–13. https://doi.org/10.1186/S40478-018-0565-6/FIGURES/5.
21. Liu, C., and Götz, J. (2013). Profiling murine tau with 0N, 1N and 2N isoform-specific antibodies in brain and peripheral organs reveals distinct subcellular localization, with the 1N isoform being enriched in the nucleus. PLoS One *8*, 1–18. https://doi.org/10.1371/journal.pone.0084849.
22. Benhelli-Mokrani, H., Mansuroglu, Z., Chauderlier, A., Albaud, B., Gentien, D., Sommer, S., Schirmer, C., Laqueuvre, L., Josse, T., Buée, L., et al. (2018). Genome-wide identification of genic and intergenic neuronal DNA regions bound by Tau protein under physiological and stress conditions. Nucleic Acids Res *46*, 11405–11422. https://doi.org/10.1093/nar/gky929.
23. Mansuroglu, Z., Benhelli-Mokrani, H., Marcato, V., Sultan, A., Violet, M., Chauderlier, A., Delattre, L., Loyens, A., Talahari, S., Bégard, S., et al. (2016). Loss of Tau protein affects the structure, transcription and repair of neuronal pericentromeric heterochromatin. Sci Rep *6*, 1–16. https://doi.org/10.1038/srep33047.
24. Abasi, L.S., Elathram, N., Movva, M., Deep, A., Corbett, K.D., and Debelouchina, G.T. (2024). Phosphorylation regulates tau's phase separation behavior and interactions with chromatin. Communications Biology 2024 7:1 *7*, 1–17. https://doi.org/10.1038/s42003-024-05920-4.
25. Rico, T., Gilles, M., Chauderlier, A., Comptdaer, T., Magnez, R., Chwastyniak, M., Drobecq, H., Pinet, F., Thuru, X., Buée, L., et al. (2018). Tau Stabilizes Chromatin Compaction. Front Cell Dev Biol *9*, 228–239. https://doi.org/10.3389/fcell.2021.740550.
26. Klein, H.U., McCabe, C., Gjoneska, E., Sullivan, S.E., Kaskow, B.J., Tang, A., Smith, R. V., Xu, J., Pfenning, A.R., Bernstein, B.E., et al. (2019). Epigenome-wide study uncovers large-scale changes in histone acetylation driven by tau pathology in aging and Alzheimer's human brains. Nat Neurosci *22*, 37–46. https://doi.org/10.1038/s41593-018-0291-1.
27. Frost, B., Bardai, F.H., and Feany, M.B. (2016). Lamin Dysfunction Mediates Neurodegeneration in Tauopathies. *26*, 129–136.
28. Wegmann, S., DeVos, S.L., Zeitler, B., Marlen, K., Bennett, R.E., Perez-Rando, M., MacKenzie, D., Yu, Q., Commins, C., Bannon, R.N., et al. (2021). Persistent repression of tau in the brain using engineered zinc finger protein transcription factors. Sci Adv *7*. https://doi.org/10.1126/SCIADV.ABE1611.
29. Padeken, J., Methot, S.P., and Gasser, S.M. (2022). Establishment of H3K9-methylated heterochromatin and its functions in tissue differentiation and maintenance. Nature Reviews Molecular Cell Biology 2022 23:9 *23*, 623–640. https://doi.org/10.1038/s41580-022-00483-w.
30. Gates, L.A., Shi, J., Rohira, A.D., Feng, Q., Zhu, B., Bedford, M.T., Sagum, C.A., Jung, S.Y., Qin, J., Tsai, M.J., et al. (2017). Acetylation on histone H3 lysine 9 mediates a switch from transcription initiation to elongation. J Biol Chem *292*, 14456. https://doi.org/10.1074/JBC.M117.802074.
31. van Steensel, B., and Belmont, A.S. (2017). Lamina-Associated Domains: Links with Chromosome Architecture, Heterochromatin, and Gene Repression. Cell *169*, 780–791. https://doi.org/10.1016/J.CELL.2017.04.022.
32. Hockings, C., Poudel, C., Feeney, K.A., Novo, C.L., Hamouda, M.S., Mela, I., Fernandez-Antoran, D., Vallejo-Ramirez, P.P., Rugg-Gunn, P.J., Chalut, K., et al. (2020). Illuminating chromatin compaction in live cells and fixed tissues using SiR-DNA fluorescence lifetime. bioRxiv, 2020.05.02.073536. https://doi.org/10.1101/2020.05.02.073536.
33. Abasi, L.S., Elathram, N., Movva, M., Deep, A., Corbett, K.D., and Debelouchina, G.T. (2024). Phosphorylation regulates tau's phase separation behavior and interactions with chromatin. Communications Biology 2024 7:1 *7*, 1–17. https://doi.org/10.1038/s42003-024-05920-4.
34. Eftekharzadeh, B., Daigle, J.G., Kapinos, L.E., Coyne, A., Schiantarelli, J., Carlomagno, Y., Cook, C., Miller, S.J., Dujardin, S., Amaral, A.S., et al. (2018). Tau Protein Disrupts

Nucleocytoplasmic Transport in Alzheimer's Disease. Neuron. https://doi.org/10.1016/j.neuron.2018.07.039.

35. Sjöberg, M.K., Shestakova, E., Mansuroglu, Z., Maccioni, R.B., and Bonnefoy, E. (2006). Tau protein binds to pericentromeric DNA: a putative role for nuclear tau in nucleolar organization. J Cell Sci *119*, 2025–2034. https://doi.org/10.1242/JCS.02907.

36. Hua, Q., He, R.Q., Haque, N., Qu, M.H., Del Carmen Alonso, A., Grundke-Iqbal, I., and Iqbal, K. (2003). Microtubule associated protein tau binds to double-stranded but not single-stranded DNA. Cell Mol Life Sci *60*, 413–421. https://doi.org/10.1007/S000180300034.

37. Qi, H., Cantrelle, F.X., Benhelli-Mokrani, H., Smet-Nocca, C., Buée, L., Lippens, G., Bonnefoy, E., Galas, M.C., and Landrieu, I. (2015). Nuclear magnetic resonance spectroscopy characterization of interaction of Tau with DNA and its regulation by phosphorylation. Biochemistry *54*, 1525–1533. https://doi.org/10.1021/BI5014613/SUPPL_FILE/BI5014613_SI_001.PDF.

38. Violet, M., Delattre, L., Tardivel, M., Sultan, A., Chauderlier, A., Caillierez, R., Talahari, S., Nesslany, F., Lefebvre, B., Bonnefoy, E., et al. (2014). A major role for Tau in neuronal DNA and RNA protection in vivo under physiological and hyperthermic conditions. Front Cell Neurosci *8*, 1–11. https://doi.org/10.3389/fncel.2014.00084.

39. Branon, T.C., Bosch, J.A., Sanchez, A.D., Udeshi, N.D., Svinkina, T., Carr, S.A., Feldman, J.L., Perrimon, N., and Ting, A.Y. (2018). Efficient proximity labeling in living cells and organisms with TurboID. Nat Biotechnol *36*, 880–898. https://doi.org/10.1038/nbt.4201.

40. Igaz, L.M., Kwong, L.K., Xu, Y., Truax, A.C., Uryu, K., Neumann, M., Clark, C.M., Elman, L.B., Miller, B.L., Grossman, M., et al. (2008). Enrichment of C-terminal fragments in TAR DNA-binding protein-43 cytoplasmic inclusions in brain but not in spinal cord of frontotemporal lobar degeneration and amyotrophic lateral sclerosis. Am J Pathol *173*, 182–194. https://doi.org/10.2353/AJPATH.2008.080003.

41. Chou, C.C., Zhang, Y.Y.J., Umoh, M.E., Vaughan, S.W., Lorenzini, I., Liu, F., Sayegh, M., Donlin-Asp, P.G., Chen, Y.H., Duong, D.M., et al. (2018). TDP-43 pathology disrupts nuclear pore complexes and nucleocytoplasmic transport in ALS/FTD. Nat Neurosci *21*, 228–239. https://doi.org/10.1038/s41593-017-0047-3.

42. Wille, H., Drewes, G., Biernat, J., Mandelkow, E.M., and Mandelkow, E. (1992). Alzheimer-like paired helical filaments and antiparallel dimers formed from microtubule-associated protein tau in vitro. J Cell Biol *118*, 573. https://doi.org/10.1083/JCB.118.3.573.

43. Zuleger, N., Robson, M.I., and Schirmer, E.C. (2011). The nuclear envelope as a chromatin organizer. Nucleus *2*, 339. https://doi.org/10.4161/NUCL.2.5.17846.

44. Bengtsson, L., and Otto, H. (2008). LUMA interacts with emerin and influences its distribution at the inner nuclear membrane. J Cell Sci *121*, 536–548. https://doi.org/10.1242/JCS.019281.

45. Schmidt, H.B., and Görlich, D. (2016). Transport Selectivity of Nuclear Pores, Phase Separation, and Membraneless Organelles. Trends Biochem Sci *41*, 46–61. https://doi.org/10.1016/j.tibs.2015.11.001.

46. Sosa, B.A., Kutay, U., and Schwartz, T.U. (2013). Structural insights into LINC complexes. Curr Opin Struct Biol *23*, 285–291. https://doi.org/10.1016/j.sbi.2013.03.005.

47. Rothballer, A., and Kutay, U. (2013). The diverse functional LINCs of the nuclear envelope to the cytoskeleton and chromatin. Chromosoma *122*, 415–429. https://doi.org/10.1007/s00412-013-0417-x.

48. Terry, L.J., Shows, E.B., and Wente, S.R. (2007). Crossing the Nuclear Envelope: Hierarchical Regulation of Nucleocytoplasmic Transport. Science (1979) *318*, 1412–1416. https://doi.org/10.1126/SCIENCE.1142204.

49. Wente, S.R., and Rout, M.P. (2010). The nuclear pore complex and nuclear transport. Cold Spring Harb Perspect Biol *2*, a000562. https://doi.org/10.1101/cshperspect.a000562.

50. Chou, C.C., Zhang, Y.Y.J., Umoh, M.E., Vaughan, S.W., Lorenzini, I., Liu, F., Sayegh, M., Donlin-Asp, P.G., Chen, Y.H., Duong, D.M., et al. (2018). TDP-43 pathology disrupts nuclear pore complexes and nucleocytoplasmic transport in ALS/FTD. Nat Neurosci *21*, 228–239. https://doi.org/10.1038/s41593-017-0047-3.

51. Carley, E., Stewart, R.K., Zieman, A., Jalilian, I., King, D.E., Zubek, A., Lin, S., Horsley, V., and King, M.C. (2021). The linc complex transmits integrin-dependent tension to the nuclear lamina and represses epidermal differentiation. Elife *10*. https://doi.org/10.7554/ELIFE.58541.

52. Sirtori, R., J. Gregoire, M., M. Potts, E., Collins, A., Donatelli, L., and Fallini, C. (2024). LINC complex alterations are a key feature of sporadic and familial ALS/FTD. Acta Neuropathol Commun *12*, 1–16. https://doi.org/10.1186/S40478-024-01778-Z/FIGURES/8.

53. Gonzalez, B.D., Billion, K., Rous, S., Pavie, B., Lange, C., and Goodchild, R. (2018). Excess LINC complexes impair brain morphogenesis in a mouse model of recessive TOR1A disease. Hum Mol Genet *27*, 2154–2170. https://doi.org/10.1093/HMG/DDY125.

54. Arsenovic, P.T., and Conway, D.E. (2018). Using Nesprin Tension Sensors to Measure Force on the LINC Complex. Methods Mol Biol *1840*, 59. https://doi.org/10.1007/978-1-4939-8691-0_6.
55. Chen, D., Bali, S., Singh, R., Wosztyl, A., Mullapudi, V., Vaquer-Alicea, J., Jayan, P., Melhem, S., Seelaar, H., van Swieten, J.C., et al. (2023). FTD-tau S320F mutation stabilizes local structure and allosterically promotes amyloid motif-dependent aggregation. Nature Communications 2023 14:1 *14*, 1–17. https://doi.org/10.1038/s41467-023-37274-6.
56. Koller, E.J., Gonzalez De La Cruz, E., MacHula, T., Ibanez, K.R., Lin, W.L., Williams, T., Riffe, C.J., Ryu, D., Strang, K.H., Liu, X., et al. (2019). Combining P301L and S320F tau variants produces a novel accelerated model of tauopathy. Hum Mol Genet *28*, 3255–3269. https://doi.org/10.1093/HMG/DDZ151.
57. Sohn, C., Ma, J., Ray, W.J., and Frost, B. (2023). Pathogenic tau decreases nuclear tension in cultured neurons. Frontiers in Aging *4*, 1–11. https://doi.org/10.3389/fragi.2023.1058968.
58. Frost, B. (2023). Alzheimer's disease and related tauopathies: disorders of disrupted neuronal identity. Trends Neurosci *46*, 797–813. https://doi.org/10.1016/j.tins.2023.07.006.
59. Paonessa, F., Evans, L.D., Solanki, R., Larrieu, D., Wray, S., Hardy, J., Jackson, S.P., and Livesey, F.J. (2019). Microtubules Deform the Nuclear Membrane and Disrupt Nucleocytoplasmic Transport in Tau-Mediated Frontotemporal Dementia. Cell Rep *26*, 582-593.e5. https://doi.org/10.1016/j.celrep.2018.12.085.
60. Bolognesi, B., Gotor, N.L., Dhar, R., Cirillo, D., Baldrighi, M., Tartaglia, G.G., and Lehner, B. (2016). A Concentration-Dependent Liquid Phase Separation Can Cause Toxicity upon Increased Protein Expression. Cell Rep *16*, 222–231. https://doi.org/10.1016/J.CELREP.2016.05.076.
61. Chen, Z., Hou, C., Wang, L., Yu, C., Chen, T., Shen, B., Hou, Y., Li, P., and Li, T. (2022). Screening membraneless organelle participants with machine-learning models that integrate multimodal features. Proc Natl Acad Sci U S A *119*, e2115369119. https://doi.org/10.1073/PNAS.2115369119/SUPPL_FILE/PNAS.2115369119.SD08.XLSX.
62. von Appen, A., LaJoie, D., Johnson, I.E., Trnka, M.J., Pick, S.M., Burlingame, A.L., Ullman, K.S., and Frost, A. (2020). LEM2 phase separation promotes ESCRT-mediated nuclear envelope reformation. Nature *582*, 115–118. https://doi.org/10.1038/s41586-020-2232-x.
63. Hernández-Vega, A., Braun, M., Scharrel, L., Jahnel, M., Wegmann, S., Hyman, B.T., Alberti, S., Diez, S., and Hyman, A.A. (2017). Local Nucleation of Microtubule Bundles through Tubulin Concentration into a Condensed Tau Phase. Cell Rep *20*, 2304–2312. https://doi.org/10.1016/J.CELREP.2017.08.042.
64. Hochmair, J., Oetelaar, M.C.M. van den, Diez, L., Lemmens, L.J.M., Ponce, R., Ravatt, L., Franck, M.W., Semenova, E., Mohapatra, S., Ottmann, C., et al. (2024). 14-3-3 binding regulates Tau assembly and microtubule association. bioRxiv, 2024.03.15.585148. https://doi.org/10.1101/2024.03.15.585148.
65. Sang, D., Shu, T., Pantoja, C.F., Ibáñez de Opakua, A., Zweckstetter, M., and Holt, L.J. (2022). Condensed-phase signaling can expand kinase specificity and respond to macromolecular crowding. *82*, 3693-3711.e10.
66. Zhou, J., Chuang, Y. 'an, Redding-Ochoa, J., Zhang, R., Platero, A.J., Barrett, A.H., Troncoso, J.C., Worley, P.F., and Zhang, W. (2024). The autophagy adaptor TRIAD3A promotes tau fibrillation by nested phase separation. Nature Cell Biology 2024 26:8 *26*, 1274–1286. https://doi.org/10.1038/s41556-024-01461-4.
67. Brachner, A., Reipert, S., Foisner, R., and Gotzmann, J. (2005). LEM2 is a novel MAN1-related inner nuclear membrane protein associated with A-type lamins. J Cell Sci *118*, 5797–5810. https://doi.org/10.1242/JCS.02701.
68. Banday, S., Farooq, Z., Rashid, R., Abdullah, E., and Altaf, M. (2016). No Title. *291*.
69. Brachner, A., Reipert, S., Foisner, R., and Gotzmann, J. (2005). LEM2 is a novel MAN1-related inner nuclear membrane protein associated with A-type lamins. J Cell Sci *118*, 5797–5810. https://doi.org/10.1242/JCS.02701.
70. King, M.R., and Petry, S. (2020). Phase separation of TPX2 enhances and spatially coordinates microtubule nucleation. Nature Communications 2020 11:1 *11*, 1–13. https://doi.org/10.1038/s41467-019-14087-0.
71. Gottschall, P.E., and Howell, M.D. (2015). ADAMTS expression and function in central nervous system injury and disorders. Matrix Biol *44–46*, 70. https://doi.org/10.1016/J.MATBIO.2015.01.014.
72. Balusu, S., Praschberger, R., Lauwers, E., De Strooper, B., and Verstreken, P. (2023). Neurodegeneration cell per cell. Neuron *111*, 767–786. https://doi.org/10.1016/J.NEURON.2023.01.016.

73. Nyati, K.K., Zaman, M.M.U., Sharma, P., and Kishimoto, T. (2020). Arid5a, an RNA-Binding Protein in Immune Regulation: RNA Stability, Inflammation, and Autoimmunity. Trends Immunol *41*, 255–268. https://doi.org/10.1016/J.IT.2020.01.004/ASSET/C0B0DD94-6C3F-4822-82F3-0CC40A4D83CA/MAIN.ASSETS/GR4.SML.
74. Guo, S., Zhu, W., Bian, Y., Li, Z., Zheng, H., Li, W., Yang, Y., Ji, X., and Zhang, B. (2024). Developing diagnostic biomarkers for Alzheimer's disease based on histone lactylation-related gene. Heliyon *10*, e37807. https://doi.org/10.1016/J.HELIYON.2024.E37807.
75. Cichocki, F., Wu, C.Y., Zhang, B., Felices, M., Tesi, B., Tuininga, K., Dougherty, P., Taras, E., Hinderlie, P., Blazar, B.R., et al. (2018). ARID5B regulates metabolic programming in human adaptive NK cells. J Exp Med *215*, 2379. https://doi.org/10.1084/JEM.20172168.
76. Varma, V.R., Büşra Lüleci, H., Oommen, A.M., Varma, S., Blackshear, C.T., Griswold, M.E., An, Y., Roberts, J.A., O'Brien, R., Pletnikova, O., et al. (2021). Abnormal brain cholesterol homeostasis in Alzheimer's disease—a targeted metabolomic and transcriptomic study. npj Aging and Mechanisms of Disease 2021 7:1 *7*, 1–14. https://doi.org/10.1038/s41514-021-00064-9.
77. Satoh, J.I., Yamamoto, Y., Asahina, N., Kitano, S., and Kino, Y. (2014). RNA-Seq Data Mining: Downregulation of NeuroD6 Serves as a Possible Biomarker for Alzheimer's Disease Brains. Dis Markers *2014*, 123165. https://doi.org/10.1155/2014/123165.
78. Yang, J., Yao, Y., Wang, L., Yang, C., Wang, F., Guo, J., Wang, Z., Yang, Z., and Ming, D. (2017). Gastrin-releasing peptide facilitates glutamatergic transmission in the hippocampus and effectively prevents vascular dementia induced cognitive and synaptic plasticity deficits. Exp Neurol *287*, 75–83. https://doi.org/10.1016/J.EXPNEUROL.2016.08.008.
79. Kawakami, E., Nakaoka, S., Ohta, T., and Kitano, H. (2016). Weighted enrichment method for prediction of transcription regulators from transcriptome and global chromatin immunoprecipitation data. Nucleic Acids Res *44*, 5010–5021. https://doi.org/10.1093/NAR/GKW355.
80. Aguado, F., Díaz-Ruiz, C., Parlato, R., Martínez, A., Carmona, M.A., Bleckmann, S., Ureña, J.M., Burgaya, F., Del Río, J.A., Schütz, G., et al. (2009). The CREB/CREM Transcription Factors Negatively Regulate Early Synaptogenesis and Spontaneous Network Activity. The Journal of Neuroscience *29*, 328. https://doi.org/10.1523/JNEUROSCI.5252-08.2009.
81. Hwang, J.Y., and Zukin, R.S. (2018). REST, a master transcriptional regulator in neurodegenerative disease. Curr Opin Neurobiol *48*, 193. https://doi.org/10.1016/J.CONB.2017.12.008.
82. Cheng, Y., Yin, Y., Zhang, A., Bernstein, A.M., Kawaguchi, R., Gao, K., Potter, K., Gilbert, H.Y., Ao, Y., Ou, J., et al. (2022). Transcription factor network analysis identifies REST/NRSF as an intrinsic regulator of CNS regeneration in mice. Nature Communications 2022 13:1 *13*, 1–22. https://doi.org/10.1038/s41467-022-31960-7.
83. McClelland, S., Brennan, G.P., Dubé, C., Rajpara, S., Iyer, S., Richichi, C., Bernard, C., and Baram, T.Z. (2014). The transcription factor NRSF contributes to epileptogenesis by selective repression of a subset of target genes. Elife *3*, e01267. https://doi.org/10.7554/ELIFE.01267.
84. Lu, T., Aron, L., Zullo, J., Pan, Y., Kim, H., Chen, Y., Yang, T.H., Kim, H.M., Drake, D., Liu, X.S., et al. (2014). REST and stress resistance in ageing and Alzheimer's disease. Nature *507*, 448–454. https://doi.org/10.1038/NATURE13163.
85. Aron, L., Qiu, C., Ngian, Z.K., Liang, M., Drake, D., Choi, J., Fernandez, M.A., Roche, P., Bunting, E.L., Lacey, E.K., et al. (2023). A neurodegeneration checkpoint mediated by REST protects against the onset of Alzheimer's disease. Nat Commun *14*. https://doi.org/10.1038/S41467-023-42704-6.
86. McClelland, S., Flynn, C., Dubé, C., Richichi, C., Zha, Q., Ghestem, A., Esclapez, M., Bernard, C., and Baram, T.Z. (2011). Neuron-restrictive silencer factor-mediated hyperpolarization-activated cyclic nucleotide gated channelopathy in experimental temporal lobe epilepsy. Ann Neurol *70*, 454–465. https://doi.org/10.1002/ANA.22479.
87. Zuccato, C., Tartari, M., Crotti, A., Goffredo, D., Valenza, M., Conti, L., Cataudella, T., Leavitt, B.R., Hayden, M.R., Timmusk, T., et al. (2003). Huntingtin interacts with REST/NRSF to modulate the transcription of NRSE-controlled neuronal genes. Nat Genet *35*, 76–83. https://doi.org/10.1038/NG1219.
88. Chuang, D.M., Leng, Y., Marinova, Z., Kim, H.J., and Chiu, C.T. (2009). Multiple roles of HDAC inhibition in neurodegenerative conditions. Trends Neurosci *32*, 591–601. https://doi.org/10.1016/J.TINS.2009.06.002.
89. Canchi, S., Raao, B., Masliah, D., Rosenthal, S.B., Sasik, R., Fisch, K.M., Jager, P. De, Bennett, D.A., and Rissman, R.A. (2018). Perturbed functional networks in Alzheimer's Disease reveal opposing roles for TGIF and EGR3. bioRxiv, 286674. https://doi.org/10.1101/286674.

90. Martínez, M., and Inestrosa, N.C. (2021). The transcriptional landscape of Alzheimer's disease and its association with Wnt signaling pathway. Neurosci Biobehav Rev *128*, 454–466. https://doi.org/10.1016/J.NEUBIOREV.2021.06.029.
91. Rylski, M., Amborska, R., Zybura, K., Michaluk, P., Bielinska, B., Konopacki, F.A., Wilczynski, G.M., and Kaczmarek, L. (2009). JunB is a repressor of MMP-9 transcription in depolarized rat brain neurons. Molecular and Cellular Neuroscience *40*, 98–110. https://doi.org/10.1016/J.MCN.2008.09.005.
92. Karin, M., and Chang, L. (2001). AP-1--glucocorticoid receptor crosstalk taken to a higher level. J Endocrinol *169*, 447–451. https://doi.org/10.1677/JOE.0.1690447.
93. Chatoo, W., Abdouh, M., David, J., Champagne, M.P., Ferreira, J., Rodier, F., and Bernier, G. (2009). The Polycomb Group Gene Bmi1 Regulates Antioxidant Defenses in Neurons by Repressing p53 Pro-Oxidant Activity. Journal of Neuroscience *29*, 529–542. https://doi.org/10.1523/JNEUROSCI.5303-08.2009.
94. Tai, X.Y., Koepp, M., Duncan, J.S., Fox, N., Thompson, P., Baxendale, S., Liu, J.Y.W., Reeves, C., Michalak, Z., and Thom, M. (2016). Hyperphosphorylated tau in patients with refractory epilepsy correlates with cognitive decline: a study of temporal lobe resections. Brain *139*, 2441–2455. https://doi.org/10.1093/BRAIN/AWW187.
95. Lopes, S., Vaz-Silva, J., Pinto, V., Dalla, C., Kokras, N., Bedenk, B., Mack, N., Czisch, M., Almeida, O.F.X., Sousa, N., et al. (2016). Tau protein is essential for stress-induced brain pathology. Proc Natl Acad Sci U S A *113*, E3755–E3763. https://doi.org/10.1073/pnas.1600953113.
96. Orr, M.E., Sullivan, A.C., and Frost, B. (2017). A Brief Overview of Tauopathy: Causes, Consequences, and Therapeutic Strategies. Trends Pharmacol Sci *38*, 637. https://doi.org/10.1016/J.TIPS.2017.03.011.
97. An, H., Williams, N.G., and Shelkovnikova, T.A. (2018). NEAT1 and paraspeckles in neurodegenerative diseases: A missing lnc found? Noncoding RNA Res *3*, 243–252. https://doi.org/10.1016/J.NCRNA.2018.11.003.
98. Chai, W.N., Wu, Y.F., Wu, Z.M., Xie, Y.F., Shi, Q.H., Dan, W., Zhan, Y., Zhong, J.J., Tang, W., Sun, X.C., et al. (2022). Neat1 decreases neuronal apoptosis after oxygen and glucose deprivation. Neural Regen Res *17*, 163–169. https://doi.org/10.4103/1673-5374.314313.
99. Morchikh, M., Cribier, A., Raffel, R., Amraoui, S., Cau, J., Severac, D., Dubois, E., Schwartz, O., Bennasser, Y., and Benkirane, M. (2017). HEXIM1 and NEAT1 Long Non-coding RNA Form a Multi-subunit Complex that Regulates DNA-Mediated Innate Immune Response. Mol Cell *67*, 387-399.e5. https://doi.org/10.1016/J.MOLCEL.2017.06.020.
100. Barry, G., Briggs, J.A., Hwang, D.W., Nayler, S.P., Fortuna, P.R.J., Jonkhout, N., Dachet, F., Maag, J.L.V., Mestdagh, P., Singh, E.M., et al. (2017). The long non-coding RNA NEAT1 is responsive to neuronal activity and is associated with hyperexcitability states. Sci Rep *7*. https://doi.org/10.1038/SREP40127.
101. Liu, S., Heumüller, S.E., Hossinger, A., Müller, S.A., Buravlova, O., Lichtenthaler, S.F., Denner, P., and Vorberg, I.M. (2023). Reactivated endogenous retroviruses promote protein aggregate spreading. Nat Commun *14*. https://doi.org/10.1038/S41467-023-40632-Z.
102. van Steensel, B., and Belmont, A.S. (2017). Lamina-associated domains: links with chromosome architecture, heterochromatin and gene repression. Cell *169*, 780. https://doi.org/10.1016/J.CELL.2017.04.022.
103. Briand, N., and Collas, P. (2020). Lamina-associated domains: Peripheral matters and internal affairs. Genome Biol *21*, 1–25. https://doi.org/10.1186/s13059-020-02003-5.
104. van Steensel, B., and Belmont, A.S. (2017). Lamina-Associated Domains: Links with Chromosome Architecture, Heterochromatin, and Gene Repression. Cell *169*, 780–791. https://doi.org/10.1016/J.CELL.2017.04.022.
105. Cremer, T., and Cremer, C. (2001). Chromosome territories, nuclear architecture and gene regulation in mammalian cells. Nature Reviews Genetics 2001 2:4 *2*, 292–301. https://doi.org/10.1038/35066075.
106. Shah, P.P., Keough, K.C., Gjoni, K., Santini, G.T., Abdill, R.J., Wickramasinghe, N.M., Dundes, C.E., Karnay, A., Chen, A., Salomon, R.E.A., et al. (2023). An atlas of lamina-associated chromatin across twelve human cell types reveals an intermediate chromatin subtype. Genome Biol *24*, 1–35. https://doi.org/10.1186/S13059-023-02849-5/FIGURES/2.
107. Manuelidis, L., and Borden, J. (1988). Reproducible compartmentalization of individual chromosome domains in human CNS cells revealed by in situ hybridization and three-dimensional reconstruction. Chromosoma *96*, 397–410. https://doi.org/10.1007/BF00303033.
108. Tanabe, H., Müller, S., Neusser, M., Von Hase, J., Calcagno, E., Cremer, M., Solovei, I., Cremer, C., and Cremer, T. (2002). Evolutionary conservation of chromosome territory

arrangements in cell nuclei from higher primates. Proc Natl Acad Sci U S A *99*, 4424–4429. https://doi.org/10.1073/pnas.072618599.

109. Borden, J., and Manuelidis, L. (1988). Movement of the X chromosome in epilepsy. Science (1979) *242*, 1686–1691. https://doi.org/10.1126/SCIENCE.3201257.

110. Earliest Stages of Tau Conformational Changes are Related to the Appearance of a Sequence of Specific Phospho-Dependent Tau Epitopes in Alzheimer's Disease | Enhanced Reader.

111. Askin, B., Gomez, C.C., Duong, S.L.-L., Kilic, C., Goihl, A., Newman, A., Wagner, J., Thomas, V., Lamberty, J., Huebschmann, S., et al. (2024). Autoimmune antibody-induced neuronal hyperactivity triggers pathological Tau in IgLON5 disease. bioRxiv, 2024.03.10.584272. https://doi.org/10.1101/2024.03.10.584272.

112. Benhelli-Mokrani, H., Mansuroglu, Z., Chauderlier, A., Albaud, B., Gentien, D., Sommer, S., Schirmer, C., Laqueuvre, L., Josse, T., Buée, L., et al. (2018). Genome-wide identification of genic and intergenic neuronal DNA regions bound by Tau protein under physiological and stress conditions. Nucleic Acids Res *46*, 11405–11422. https://doi.org/10.1093/nar/gky929.

113. Wang, C., Fan, L., Khawaja, R.R., Liu, B., Zhan, L., Kodama, L., Chin, M., Li, Y., Le, D., Zhou, Y., et al. (2022). Microglial NF-κB drives tau spreading and toxicity in a mouse model of tauopathy. Nature Communications 2022 13:1 *13*, 1–19. https://doi.org/10.1038/s41467-022-29552-6.

114. Shin, K.C., Ali Moussa, H.Y., and Park, Y. (2024). Cholesterol imbalance and neurotransmission defects in neurodegeneration. Experimental & Molecular Medicine 2024 56:8 *56*, 1685–1690. https://doi.org/10.1038/s12276-024-01273-4.

115. Mailman, T., Hariharan, M., and Karten, B. (2011). Inhibition of neuronal cholesterol biosynthesis with lovastatin leads to impaired synaptic vesicle release even in the presence of lipoproteins or geranylgeraniol. J Neurochem *119*, 1002–1015. https://doi.org/10.1111/J.1471-4159.2011.07474.X.

116. Koudinov, A.R., and Koudinova, N. V. (2001). Essential role for cholesterol in synaptic plasticity and neuronal degeneration. FASEB J *15*, 1858–1860. https://doi.org/10.1096/FJ.00-0815FJE.

117. Li, D., Zhang, J., and Liu, Q. (2022). Brain cell type-specific cholesterol metabolism and implications for learning and memory. Trends Neurosci *45*, 401–414. https://doi.org/10.1016/J.TINS.2022.01.002.

118. Jiang, L., and Wolozin, B. (2021). Oligomeric tau disrupts nuclear envelope via binding to lamin proteins and lamin B receptor. Alzheimer's & Dementia *17*, e054521. https://doi.org/10.1002/ALZ.054521.

119. Brachner, A., Reipert, S., Foisner, R., and Gotzmann, J. (2005). LEM2 is a novel MAN1-related inner nuclear membrane protein associated with A-type lamins. J Cell Sci *118*, 5797–5810. https://doi.org/10.1242/JCS.02701.

120. Olins, A.L., Rhodes, G., Welch, D.B.M., Zwerger, M., and Olins, D.E. (2010). Lamin B receptor. Nucleus *1*, 53–70. https://doi.org/10.4161/NUCL.1.1.10515.

121. Frost, B. (2016). Alzheimer's disease: An acquired neurodegenerative laminopathy. Preprint at Taylor & Francis, https://doi.org/10.1080/19491034.2016.1183859 https://doi.org/10.1080/19491034.2016.1183859.

122. Frost, B., Bardai, F.H., and Feany, M.B. (2016). Lamin Dysfunction Mediates Neurodegeneration in Tauopathies. *26*, 129–136.

123. Nava, M.M., Miroshnikova, Y.A., Biggs, L.C., Whitefield, D.B., Metge, F., Boucas, J., Vihinen, H., Jokitalo, E., Li, X., García Arcos, J.M., et al. (2020). Heterochromatin-Driven Nuclear Softening Protects the Genome against Mechanical Stress-Induced Damage. Cell *181*, 800-817.e22. https://doi.org/10.1016/J.CELL.2020.03.052.

124. Carley, E., Stewart, R.K., Zieman, A., Jalilian, I., King, D.E., Zubek, A., Lin, S., Horsley, V., and King, M.C. (2021). The linc complex transmits integrin-dependent tension to the nuclear lamina and represses epidermal differentiation. Elife *10*. https://doi.org/10.7554/ELIFE.58541.

125. Janin, A., Bauer, D., Ratti, F., Millat, G., and Méjat, A. (2017). Nuclear envelopathies: A complex LINC between nuclear envelope and pathology. Orphanet J Rare Dis *12*, 1–16. https://doi.org/10.1186/s13023-017-0698-x.

126. Sirtori, R., J. Gregoire, M., M. Potts, E., Collins, A., Donatelli, L., and Fallini, C. (2024). LINC complex alterations are a key feature of sporadic and familial ALS/FTD. Acta Neuropathol Commun *12*. https://doi.org/10.1186/S40478-024-01778-Z.

127. Yang, L., Munck, M., Swaminathan, K., Kapinos, L.E., Noegel, A.A., and Neumann, S. (2013). Mutations in LMNA Modulate the Lamin A - Nesprin-2 Interaction and Cause LINC Complex Alterations. PLoS One *8*. https://doi.org/10.1371/journal.pone.0071850.

128. Kay, K.R., Smith, C., Wright, A.K., Serrano-Pozo, A., Pooler, A.M., Koffie, R., Bastin, M.E., Bak, T.H., Abrahams, S., Kopeikina, K.J., et al. (2013). Studying synapses in human brain with

array tomography and electron microscopy. Nat Protoc *8*, 1366–1380. https://doi.org/10.1038/NPROT.2013.078.

129. Dobin, A., Davis, C.A., Schlesinger, F., Drenkow, J., Zaleski, C., Jha, S., Batut, P., Chaisson, M., and Gingeras, T.R. (2013). STAR: ultrafast universal RNA-seq aligner. Bioinformatics *29*, 15–21. https://doi.org/10.1093/BIOINFORMATICS/BTS635.
130. Jin, Y., Tam, O.H., Paniagua, E., and Hammell, M. (2015). TEtranscripts: a package for including transposable elements in differential expression analysis of RNA-seq datasets. Bioinformatics *31*, 3593–3599. https://doi.org/10.1093/BIOINFORMATICS/BTV422.
131. Durinck, S., Spellman, P.T., Birney, E., and Huber, W. (2009). Mapping identifiers for the integration of genomic datasets with the R/Bioconductor package biomaRt. Nat Protoc *4*, 1184–1191. https://doi.org/10.1038/NPROT.2009.97.
132. Love, M.I., Huber, W., and Anders, S. (2014). Moderated estimation of fold change and dispersion for RNA-seq data with DESeq2. Genome Biol *15*, 1–21. https://doi.org/10.1186/S13059-014-0550-8/FIGURES/9.
133. Ignatiadis, N., Klaus, B., Zaugg, J.B., and Huber, W. (2016). Data-driven hypothesis weighting increases detection power in genome-scale multiple testing. Nat Methods *13*, 577–580. https://doi.org/10.1038/NMETH.3885.
134. Zhu, A., Ibrahim, J.G., and Love, M.I. (2019). Heavy-tailed prior distributions for sequence count data: removing the noise and preserving large differences. Bioinformatics *35*, 2084–2092. https://doi.org/10.1093/BIOINFORMATICS/BTY895.
135. Korotkevich, G., Sukhov, V., Budin, N., Shpak, B., Artyomov, M.N., and Sergushichev, A. (2021). Fast gene set enrichment analysis. bioRxiv, 060012. https://doi.org/10.1101/060012.
136. Ashburner, M., Ball, C.A., Blake, J.A., Botstein, D., Butler, H., Cherry, J.M., Davis, A.P., Dolinski, K., Dwight, S.S., Eppig, J.T., et al. (2000). Gene Ontology: tool for the unification of biology. Nature Genetics 2000 25:1 *25*, 25–29. https://doi.org/10.1038/75556.
137. Carbon, S., Douglass, E., Good, B.M., Unni, D.R., Harris, N.L., Mungall, C.J., Basu, S., Chisholm, R.L., Dodson, R.J., Hartline, E., et al. (2021). The Gene Ontology resource: enriching a GOld mine. Nucleic Acids Res *49*, D325–D334. https://doi.org/10.1093/NAR/GKAA1113.
138. Subramanian, A., Tamayo, P., Mootha, V.K., Mukherjee, S., Ebert, B.L., Gillette, M.A., Paulovich, A., Pomeroy, S.L., Golub, T.R., Lander, E.S., et al. (2005). Gene set enrichment analysis: A knowledge-based approach for interpreting genome-wide expression profiles. Proc Natl Acad Sci U S A *102*, 15545–15550. https://doi.org/10.1073/PNAS.0506580102/SUPPL_FILE/06580FIG7.JPG.
139. Liberzon, A., Birger, C., Thorvaldsdóttir, H., Ghandi, M., Mesirov, J.P., and Tamayo, P. (2015). The Molecular Signatures Database (MSigDB) hallmark gene set collection. Cell Syst *1*, 417–425. https://doi.org/10.1016/J.CELS.2015.12.004.
140. Schwarz, R., Koch, P., Wilbrandt, J., and Hoffmann, S. (2022). Locus-specific expression analysis of transposable elements. Brief Bioinform *23*. https://doi.org/10.1093/BIB/BBAB417.
141. Jeong, H.H., Yalamanchili, H.K., Guo, C., Shulman, J.M., and Liu, Z. (2018). An ultra-fast and scalable quantification pipeline for transposable elements from next generation sequencing data. Pacific Symposium on Biocomputing *0*, 168–179. https://doi.org/10.1142/9789813235533_0016.
142. Love, M.I., Huber, W., and Anders, S. (2014). Moderated estimation of fold change and dispersion for RNA-seq data with DESeq2. Genome Biol *15*, 1–21. https://doi.org/10.1186/S13059-014-0550-8/FIGURES/9.
143. Lawrence, M., Huber, W., Pagès, H., Aboyoun, P., Carlson, M., Gentleman, R., Morgan, M.T., and Carey, V.J. (2013). Software for Computing and Annotating Genomic Ranges. PLoS Comput Biol *9*, e1003118. https://doi.org/10.1371/JOURNAL.PCBI.1003118.
144. Sakurai, K., Morita, M., Aomine, Y., Matsumoto, M., Moriyama, T., Kasahara, E., Sekiyama, A., Otani, M., Oshima, R., Loveland, K.L., et al. (2024). Importin α4 deficiency induces psychiatric disorder-related behavioral deficits and neuroinflammation in mice. Translational Psychiatry 2024 14:1 *14*, 1–10. https://doi.org/10.1038/s41398-024-03138-w.
145. Langmead, B., and Salzberg, S.L. (2012). Fast gapped-read alignment with Bowtie 2. Nature Methods 2012 9:4 *9*, 357–359. https://doi.org/10.1038/nmeth.1923.
146. Meers, M.P., Tenenbaum, D., and Henikoff, S. (2019). Peak calling by Sparse Enrichment Analysis for CUT&RUN chromatin profiling. Epigenetics Chromatin *12*, 1–11. https://doi.org/10.1186/S13072-019-0287-4/FIGURES/6.
147. Schep, A.N., Wu, B., Buenrostro, J.D., and Greenleaf, W.J. (2017). chromVAR: inferring transcription-factor-associated accessibility from single-cell epigenomic data. Nature Methods 2017 14:10 *14*, 975–978. https://doi.org/10.1038/nmeth.4401.